Structure–function analyses of the G729R 2-oxoadipate dehydrogenase genetic variant associated with a disorder of L-lysine metabolism

Received for publication, January 22, 2020, and in revised form, April 16, 2020 Published, Papers in Press, April 17, 2020, DOI 10.1074/jbc.RA120.012761

Xu Zhang[‡1], Natalia S. Nemeria[‡1,2], João Leandro[§], Sander Houten[§3], Michael Lazarus[§], Gary Gerfen[¶], Oliver Ozohanics[‖], Attila Ambrus[‖], Balint Nagy[‖], Roman Brukh[‡], and Frank Jordan[‡4]

From the [‡]Department of Chemistry, Rutgers, The State University of New Jersey, Newark, New Jersey 07102, the [§]Department of Genetics and Genomic Sciences, Icahn School of Medicine at Mount Sinai, New York, New York 10029, the [¶]Department of Physiology and Biophysics, Albert Einstein College of Medicine, Bronx, New York 10641-2304, and the [‖]Department of Medical Biochemistry, MTA-SE Laboratory for Neurobiochemistry, Semmelweis University, Budapest H-1094, Hungary

Edited by F. Peter Guengerich

2-Oxoadipate dehydrogenase (E1a, also known as DHTKD1, dehydrogenase E1, and transketolase domain-containing protein 1) is a thiamin diphosphate-dependent enzyme and part of the 2-oxoadipate dehydrogenase complex (OADHc) in L-lysine catabolism. Genetic findings have linked mutations in the *DHTKD1* gene to several metabolic disorders. These include α-aminoadipic and α-ketoadipic aciduria (AMOXAD), a rare disorder of L-lysine, L-hydroxylysine, and L-tryptophan catabolism, associated with clinical presentations such as developmental delay, mild-to-severe intellectual disability, ataxia, epilepsy, and behavioral disorders that cannot currently be managed by available treatments. A heterozygous missense mutation, c.2185G→A (p.G729R), in *DHTKD1* has been identified in most AMOXAD cases. Here, we report that the G729R E1a variant when assembled into OADHc *in vitro* displays a 50-fold decrease in catalytic efficiency for NADH production and a significantly reduced rate of glutaryl-CoA production by dihydrolipoamide succinyl-transferase (E2o). However, the G729R E1a substitution did not affect any of the three side-reactions associated solely with G729R E1a, prompting us to determine the structure–function effects of this mutation. A multipronged systematic analysis of the reaction rates in the OADHc pathway, supplemented with results from chemical cross-linking and hydrogen–deuterium exchange MS, revealed that the c.2185G→A *DHTKD1* mutation affects E1a–E2o assembly, leading to impaired channeling of OADHc intermediates. Cross-linking between the C-terminal region of both E1a and G729R E1a with the E2o lipoyl and core domains suggested that correct positioning of the C-terminal E1a region is essential for the intermediate channeling. These findings may inform the development of interventions to counter the effects of pathogenic *DHTKD1* mutations.

Genetic findings have linked the *DHTKD1* gene encoding the 2-oxoadipate (OA)[5] dehydrogenase (E1a, also known as DHTKD1, dehydrogenase E1, and transketolase domain-containing protein 1) in the L-lysine degradation pathway to pathogenesis of several metabolic disorders: AMOXAD (1–3), Charcot-Marie-Tooth disease type 2Q (CMT2Q) (4–6), and eosinophilic esophagitis (EoE), a chronic allergic disorder (7). A pharmacological inhibition of E1a has been proposed as a strategy to treat glutaric aciduria type 1, a metabolic disorder that is caused by mutations in the *GCDH* gene encoding the mitochondrial protein glutaryl-CoA dehydrogenase (GCDH) located downstream of the E1a in the L-lysine degradation pathway (8, 9). A heterozygous missense mutation (c.2185G→A (p.G729R)) has been identified in a majority of cases with AMOXAD and is predicted to be disease-causing (1–3). The population frequency of the c.2185G→A (p. G729R) *DHTKD1* variant may approach one in 600 individuals (465 of 279,662 chromosomes in the genome Aggregation Database (gnomAD)). The genetic association of the (c.2185G→A (p. G729R)) *DHTKD1* mutation with the biochemical phenotype of AMOXAD has been established in complementation exper-

This work was supported by National Institutes of Health Grants 9R15GM116077-01 (to F. J.), R03HD092878 (to S. H.), and R21HD088775 (to S. H.); National Science Foundation Grants CHE-1402675 (to F. J.) and CHE-1213550 (to G. G.); the Rutgers-Newark Chancellor's SEED grant (to F. J.); Hungarian Higher Education Institution Excellence Program FIKP61826 690289 EATV (to A. A); and an Erasmus grant from the European Union (to A. A. and F. J.). The authors declare that they have no conflicts of interest with the contents of this article. The content is solely the responsibility of the authors and does not necessarily represent the official views of the National Institutes of Health.

This article contains Figs. S1–S10, Tables S1–S5, and supporting Refs. 1 and 2.

[1] Both authors contributed equally to this work.

[2] To whom correspondence may be addressed. E-mail: nemerianatalia@gmail.com.

[3] To whom correspondence may be addressed. E-mail: sander.houten@mssm.edu.

[4] To whom correspondence may be addressed. Tel.: 973-353-5470; Fax: 973-353-1264; E-mail: frjordan@rutgers.edu.

[5] The abbreviations used are: OA, 2-oxoadipate; OADHc, 2-oxoadipate dehydrogenase complex; OGDHc, 2-oxoglutarate dehydrogenase complex; E1o, 2-oxoglutarate dehydrogenase; E1a, 2-oxoadipate dehydrogenase; E2o, dihydrolipoamide succinyltransferase; E3, dihydrolipoamide dehydrogenase; LDo, lipoyl domain; CDo, E2o catalytic domain; GCDH, glutaryl-CoA dehydrogenase; AMOXAD, α-aminoadipic and α-ketoadipic aciduria; CMT2Q, Charcot-Marie-Tooth disease type 2Q; EoE, eosinophilic esophagitis; OG, 2-oxoglutarate; ROS, reactive oxygen species; TCA cycle, tricarboxylic acid cycle; ThDP, thiamin diphosphate; HDX–MS, hydrogen/deuterium exchange mass spectrometry; CL–MS, chemical cross-linking mass spectrometry; FT–MS, Fourier transform mass spectrometry; MALDI-TOF, matrix-assisted laser desorption/ionization; CS, citrate synthase; CDI, 1,1′-carbonyldiimidazole cross-linker; PDB, Protein Data Bank; H/D, H/D exchange; FDR, false discovery rate.

iments by using fibroblast cell lines derived from individuals with the (c.2185G→A, p.G729R) *DHTKD1* mutation (1, 3). Also, the recent findings by Xu *et al.* (6) provided evidence for a novel relationship between AMOXAD and inherited peripheral neuropathy associated with CMT2Q, in addition to a mitochondrial dysfunction reported by these authors earlier (5). However, the molecular mechanisms leading to the pathogenesis of metabolic disorders associated with *DHTKD1* mutations are poorly understood, as is the function of the 2-oxoadipate dehydrogenase complex (OADHc) in the L-lysine degradation pathway.

It has been assumed that similar to the mitochondrial 2-oxoglutarate (OG) dehydrogenase complex (OGDHc, also known as the α-ketoglutarate dehydrogenase complex, M_r of 5×10^6) in the tricarboxylic acid (TCA) cycle, the thiamin diphosphate (ThDP)-dependent E1a (an α_2 homodimer; EC 1.2.4.2; 103.077 Da/per monomer) is the first component of the OADHc, which along with its specific dihydrolipoamide glutaryltransferase (E2a, so far unidentified gene localization) and dihydrolipoamide dehydrogenase (E3) carry out the principal reactions for glutaryl-CoA formation according to the overall reaction in Equation 1 and detailed chemistry in Equations 2–5 as follows:

$$\text{2-oxoadipate} + \text{NAD}^+ + \text{CoA} \rightarrow \text{glutaryl-CoA} + \text{NADH} + \text{H}^+ + \text{CO}_2 \quad \text{(Eq. 1)}$$

$$\text{2-oxoadipate} + \text{E1a} \rightarrow \text{C2-(}\alpha\text{-hydroxy)-}\delta\text{-carboxybutylidene-ThDP-E1a (the enamine intermediate)} + \text{CO}_2 \quad \text{(Eq. 2)}$$

$$\text{C2-(}\alpha\text{-hydroxy)-}\delta\text{-carboxybutylidene-ThDP-E1a} + \text{lipoyl-E2o} \rightarrow \textit{S}\text{8-glutaryldihydrolipoyl-E2o (reductive glutarylation)} \quad \text{(Eq. 3)}$$

$$\textit{S}\text{8-glutaryldihydrolipoyl-E2o} + \text{CoA} \rightarrow \text{glutaryl-CoA} + \text{dihydrolipoyl-E2o} \quad \text{(Eq. 4)}$$

$$\text{dihydrolipoyl-E2o} + \text{E3} + \text{NAD}^+ \rightarrow \text{lipoyl-E2o} + \text{NADH} + \text{H}^+ \quad \text{(Eq. 5)}$$

Our recent *in vitro* studies led to the remarkable recognition that E1a could recruit the dihydrolipoamide succinyltransferase (E2o) and E3 components of the OGDHc for its function; however, the assembled OGDHc and OADHc are not functionally redundant (10, 11). Each complex displayed preference for its own substrate in accord with its function in the TCA cycle and in the L-lysine degradation pathway. Our further studies *in vivo* point to the existence of a hybrid 2-oxo acid dehydrogenase complex, in which both E1a and E1o participate along with E2o and E3 (9). A cross-talk between the OGDHc in the TCA cycle and OADHc in L-lysine catabolism was suggested to be of potential relevance to EoE (7). Whole-exome sequencing and rare variant burden analysis revealed an overabundance of putative, potentially damaging *DHTKD1* mutations in multiple individuals with EoE, implicating *DHTKD1* in the genetic etiology of EoE (7). The authors also identified seven potentially-damaging genetic variants in the *DHTKD1* homologue *OGDHL*, which encoded a putative 2-oxoglutarate dehydrogenase–like protein (7). It was suggested that mutations in both *DHTKD1* and *OGDHL*, and their role in impaired mitochondrial function, are molecular pathways linked to progression of allergic inflammation (7).

Using multiple approaches, we herein unravel the effect of the common (c.2185G→A, p.G729R) *DHTKD1* mutation on protein–protein interactions in the human OADHc. Our major findings are as follows. The G729R E1a substitution does not affect the rate of OA decarboxylation in Equation 2, or the rates of the E1a–ThDP–enamine's three side-reactions (including reactive oxygen species (ROS) production). Rather, the bulk of the rate reduction in NADH production with the G729R E1a substitution ($k_{\text{cat, NADH}}$ ~24-fold lower compared with E1a) is the result of the slower rate of glutaryl transfer from the *S*8-glutaryldihydrolipoyl-E2o to CoA ($k_{\text{glutaryl-CoA}}$ ~37-fold slower compared with E1a) in Equation 4. Hydrogen/deuterium exchange MS (HDX–MS) and chemical cross-linking MS (CL–MS) revealed local conformational changes induced by the G729R E1a substitution in its C-terminal region that could affect E1a–E2o interactions. The HDX–MS experiments indicate that the interaction of E1a with E2o did not induce large-scale conformational changes in E1a; however, local backbone amide proton perturbations were indeed observed in the N-terminal region, the ThDP and Mg^{2+}-binding fold, and in the C-terminal region. In contrast, the HDX–MS data provide no clear evidence for major changes in deuterium uptake upon binding of G729R E1a to E2o at any hydrogen exchange time. The great number of cross-links formed between the C-terminal region of both E1a and G729R E1a with the E2o lipoyl domain (LDo) and E2o core domain (CDo) suggested that a correct positioning of the C-terminal region of E1a with E2o is essential for intermediate channeling in OADHc.

Results and discussion

G729R E1a is expressed in patient-derived fibroblasts with α-aminoadipic and α-ketoadipic aciduria

The compound heterozygous common mutation (c.2185A→G (p. G729R)) in *DHTKD1* was identified in a few cases with AMOXAD and is predicted to be disease-causing; however, the mechanisms of disease are poorly understood (1, 3). Earlier, we reported four cases that were heterozygous for this mutation (3). The *DHTKD1* mRNA expression levels were reported as normal; however, the level of the *DHTKD1*-encoded E1a protein was low or undetectable suggesting that the protein level could be affected. We have reinvestigated E1a protein expression using primary antibodies against E1a (GeneTex Inc., Irvine, CA) (Fig. 1). It was found that fibroblasts from an individual that carried a heterozygous (c.2185A→G (p.G729R) and WT) *DHTKD1* mutation had a normal level of E1a expression compared with that in control fibroblasts (Fig. 1*A*) (3). A lower level of E1a expression was revealed in the case compound heterozygous for the (c.2185A→G (p.G729R) and c.86dup (p.Y63IfsX3)) *DHTKD1* mutations (Fig. 1*A*); however, the protein level was detectable. Here, we also studied E1a protein

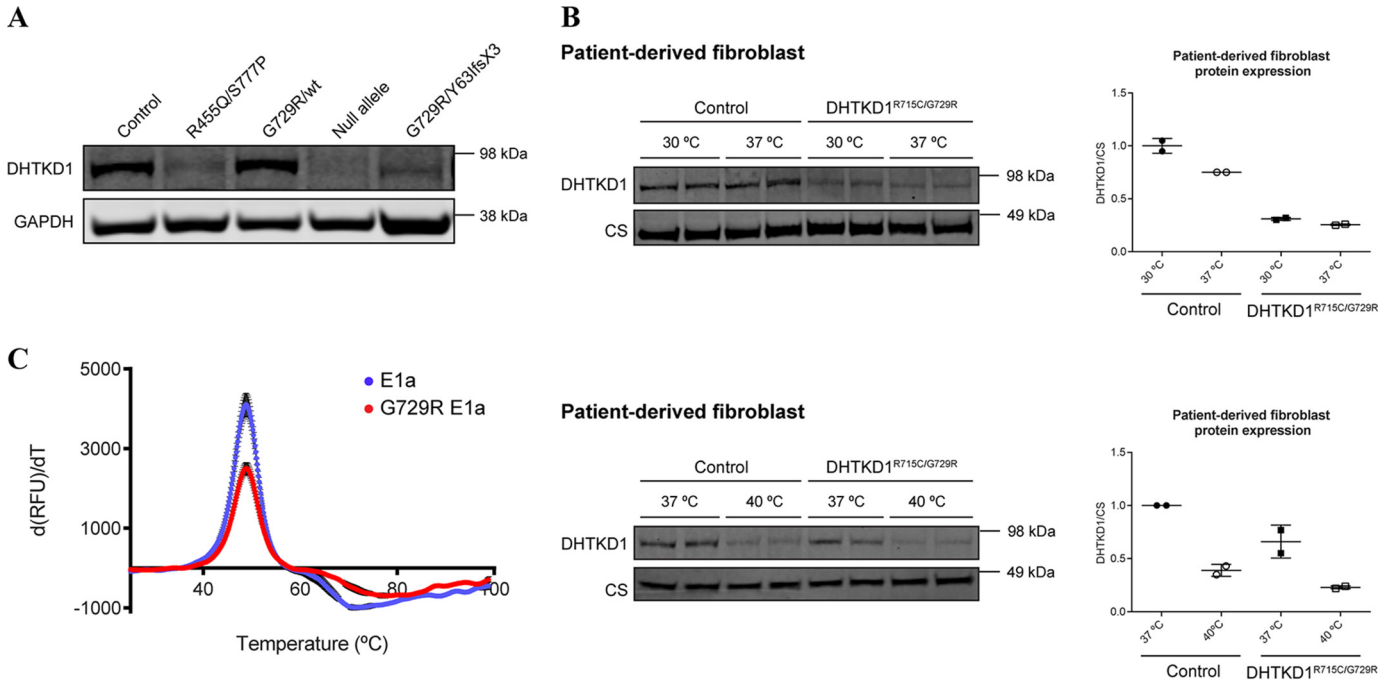

Figure 1. Characterization of the *DHTKD1*-encoded E1a levels in patient-derived fibroblasts and their thermal stability. *A,* immunoblot analysis of *DHTKD1*-encoded E1a levels in patient-derived fibroblasts. For detailed information on patient-derived fibroblasts, see Ref. 3. The E1a expression in mouse liver was used as a positive control. For null allele, the E1a protein was not detected because of the premature stop codon in *DHTKD1*. *GAPDH* denotes glyceraldehyde 3-phosphate dehydrogenase. *B,* immunoblot analysis and quantification of *DHTKD1*-encoded E1a levels in control and in patient-derived fibroblasts with R715C/G729R E1a substitution. *Top,* immunoblot analysis and quantification of *DHTKD1*-encoded E1a levels at 30 and 37 °C. *CS* denotes citrate synthase. Expression was normalized using CS. The average E1a/CS for control fibroblasts at 30 °C was set to 1. *Bottom,* immunoblot analysis and quantification of *DHTKD1*-encoded E1a levels at 37 and 40 °C. The average E1a/CS for control at 37 °C was set to 1. *Error bars* indicate S.D. The molecular mass standards are indicated on immunoblots. *C,* thermal stabilities of E1a and G729R E1a (see under "Experimental procedures: for details).

expression in fibroblasts of a case compound heterozygous for (c.2143C→T (p.R715C) and c.2185A→G (p.G729R)) *DHTKD1* (Fig. 1*B*). To evaluate whether the (c.2143C→T (p.R715C) and c.2185A→G (p.G729R)) *DHTKD1* mutations rendered the E1a$^{R715C/G729R}$ protein level temperature-sensitive, we cultured the fibroblasts as well as control fibroblasts at 30, 37, and 40 °C (Fig. 1*B*). The E1a$^{R715C/G729R}$ protein expression was lower in the *DHTKD1*-deficient cell line, but it was not temperature-sensitive (Fig. 1*B*). The data clearly indicated that on (c.2185A→G (p.G729R)) *DHTKD1* mutation, the E1a protein is expressed at a detectable level.

Thermal shift analysis of the purified recombinant E1a and G729R E1a proteins was used to determine whether the G729R E1a substitution affects protein stability (Fig. 1*C*). The calculated values of T_m = 48.85 ± 0.12 °C (E1a) and of T_m = 48.87 ± 0.0 °C (G729R E1a) were similar. This demonstration not only ruled out a stability issue being the source of the pathogenicity for the G729R E1a protein, but it also ruled out the concept of a misfolding disease resulting from the G729R E1a substitution. We next characterized the functional consequences of the c.2185G→A *DHTKD1* mutation on the encoded G729R E1a protein.

G729R E1a substitution affects the overall OADHc activity but not the E1-specific activity or any of the three side-reactions emanating from the E1a–ThDP–enamine intermediate

There are several intermediates on the pathway in Scheme 1 converting OA to glutaryl-CoA, those covalently bound to ThDP on the E1a and *S*8-glutaryldihydrolipoyl-E2o. Below, the fate of each intermediate and product will be compared for E1a and G729R E1a to help pinpoint the origin of the rate reduction produced by the pathogenic substitution. Our recent findings revealed that the E1a has recruited the E2o component of the TCA cycle OGDHc for its function in the L-lysine degradation pathway generating glutaryl-CoA (10–12). Although the E3 component is also essential for this function, the same E3 enzyme serves all such 2-oxo acid dehydrogenase complexes in a given cell; hence, its participation is less surprising.

First, it was determined that the G729R E1a variant assembled with E2o and E3 into OADHc catalyzes the conversion of OA and NAD^+ to glutaryl-CoA and NADH ($+H^+$) according to the overall reaction in Equation 1 and Scheme 1. Indeed, the catalytic efficiency of the G729RE1a of 7.7 × 10^3 M^{-1} s^{-1} was ~50-fold smaller than that for E1a, whereas similar values of $K_{m,\,OA}$ were determined in the overall NADH assay (Table 1). Next, an E1-specific kinetic assay was employed using an external chromophoric two-electron acceptor 2,6-dichlorophenolindophenol to replace E2o and E3, and this led to similar E1-specific activities of E1a (0.82 ± 0.19 μmol·min^{-1}·mg $E1a^{-1}$) and G729R E1a (0.67 ± 0.13 μmol· min^{-1}·mg G729R $E1a^{-1}$). It was therefore concluded that the G729R E1a substitution did not affect the rate of decarboxylation of the OA, *i.e.* the formation of the E1a–ThDP–enamine intermediate (Equation 2, Scheme 1, and Table 1).

In the absence of E2o and E3, the E1a–ThDP–enamine intermediate has three alternate pathways (see Scheme 1, *lower right-hand quadrant* for E1a–ThDP–enamine side-reactions),

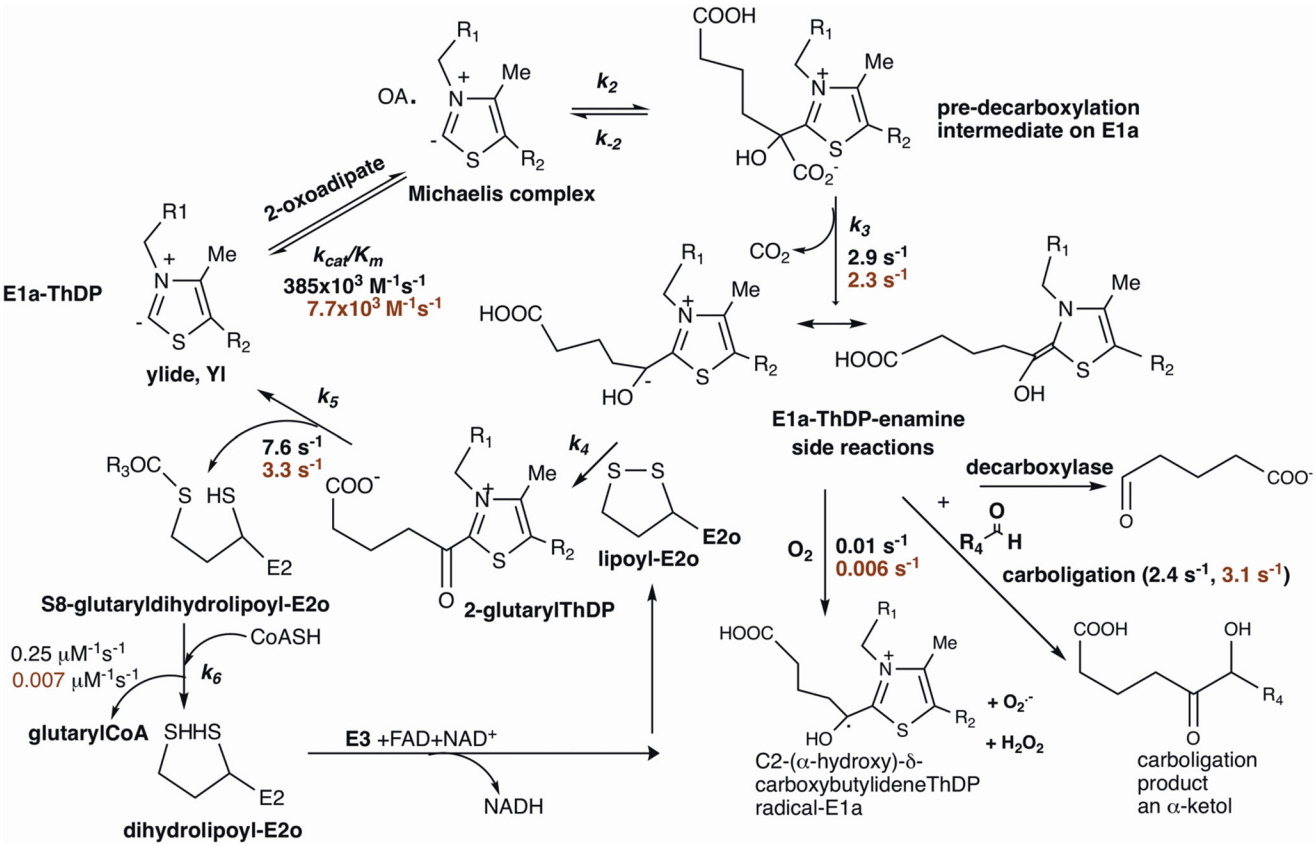

Scheme 1. Proposed mechanism for the OADHc. The kinetic parameters from Table 1 are presented for E1a (*black*) and for G729R E1a (*red*) assembled with E2o and E3 into OADHc.

Table 1
Kinetic parameters for E1a and for G729R E1a in different assays

Protein	Overall NADH assay[a]	k_{cat}/K_m[b]	E1a-specific assay	k_{cat}/K_m[c]
	$\mu mol \cdot min^{-1} \cdot mg\ E1a^{-1}$	$M^{-1}\ s^{-1}$	$\mu mol \cdot min^{-1} \cdot mg\ E1a^{-1}$	$M^{-1}\ s^{-1}$
E1a	1.38 ± 0.25 (k_{cat} = 4.8 ± 0.9 s^{-1})	385 × 10³	0.82 ± 0.19 (k_{cat} = 2.9 ± 0.7 s^{-1})	242 × 10³
G729R	0.058 ± 0.016 (k_{cat} = 0.20 ± 0.06 s^{-1})	7.7 × 10³	0.67 ± 0.13 (k_{cat} = 2.31 ± 0.46 s^{-1})	289 × 10³
Protein	**H_2O_2 assay**	**k_{cat}/K_m**	**Carbo-ligation assay**	**k_{cat}/K_m**
	$nmol \cdot min^{-1} \cdot mg\ E1a^{-1}$	$M^{-1}\ s^{-1}$	$\mu mol \cdot min^{-1} \cdot mg\ E1a^{-1}$	$M^{-1} s^{-1}$
E1a	2.85 ± 0.25 (k_{cat} = 0.01 ± 0.001 s^{-1})	2.67 × 10³	0.694 ± 0.103 (k_{cat} = 2.41 ± 0.36 s^{-1})	9.6 × 10³
G729R	1.61 ± 0.27 (k_{cat} = 0.006 ± 0.001 s^{-1})	1.47 × 10³	0.901 ± 0.090 (k_{cat} = 3.13 ± 0.31 s^{-1})	12.2 × 10³
Protein	**Glutaric semialdehyde assay**	**$LDo_{glutaryl}$, $k_{glutaryl}$**	**Glutaryl–CoA assay[d]**	
	$nmol \cdot min^{-1} \cdot mg\ E1a^{-1}$	s^{-1}	k, $\mu M^{-1}\ s^{-1}$	
E1a	6.05 ± 0.46 (k_{cat} = 0.021 ± 0.002 s^{-1})	7.6	0.245	
G729R	5.5 ± 0.15 (k_{cat} = 0.019 ± 0.001 s^{-1})	3.3	0.007	

[a] E1a and G729R E1a were assembled with E2o and E3 into OADHc.
[b] The $K_{m,\,OA}$ = 0.0124 mM (E1a) and the $K_{m,\,OA}$ = 0.026 mM (G729R E1a) values were calculated in the overall NADH assay.
[c] $K_{m,\,OA}$ = 0.012 mM (E1a) and $K_{m,\,OA}$ = 0.008 mM (G729R E1a) values were calculated in the E1-specific assay.
[d] The second-order rate constants are shown. Errors represent S.D. (n = 6).

two nonoxidative and the third oxidative, and all three scenarios have precedents in ThDP enzymology.

The simplest side-reaction (the result of C2α-protonation of the enamine) is conversion of E1a to a 2-oxoadipate decarboxylase, yielding glutaric semialdehyde from a nonoxidative decarboxylation. The rate of formation of glutaric semialdehyde by G729R E1a was also unaltered compared with E1a and could not be considered an efficient E1a side-reaction (Table 1).

The second side-reaction is carboligation (as exemplified by 2-hydroxy-3-oxoadipate synthase, which condenses OG with glyoxylate in *Mycobacterium tuberculosis* (13)). In this side-reaction, the E1a–ThDP–enamine intermediate formed on decarboxylation of OA adds to an aldehyde acceptor such as glyoxylate to form (*S*)-2-hydroxy-3-oxoheptanedioic acid, a chiral α-ketol carboligation product. The rates of 2-oxoadipate: glyoxylate carboligase activity of the E1a and G729R E1a mea-

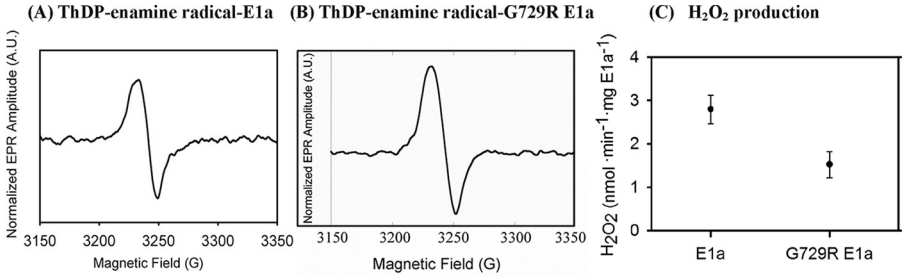

Figure 2. Generation of the ThDP-enamine radical species and H_2O_2 by E1a and by G729R E1a from 2-oxoadipate. *A,* X-band EPR spectrum of the ThDP-enamine radical species on E1a from OA as reported earlier (11). *B,* X-band EPR spectrum of the ThDP-enamine radical species observed on G729R E1a from OA. G729R E1a (29.8 mg/ml, concentration of active centers of 289 μM) in 100 mM HEPES (pH 7.5) containing 0.15 M NaCl, 0.5 mM ThDP, 2.0 mM $MgCl_2$, and 5% glycerol was mixed with 10 mM OA aerobically. The mixture was immediately transferred into an EPR tube and was flash-frozen in liquid nitrogen after ~30–40 s of incubation with 2-oxoadipate. *C,* H_2O_2 activities of the E1a and G729R E1a. The rate of H_2O_2 production by E1a and by G729R E1a assembled to OADHc was measured as reported earlier (12, 14, 15). Each value represents the mean ± S.D. ($n = 4$).

sured by circular dichroism (CD) at 280 nm (a signature for chiral α-ketols) were similar according to their calculated catalytic efficiencies: $k_{cat}/K_{m,\,OA} = 9.6 \times 10^3\ M^{-1}\ s^{-1}$ (E1a) and $k_{cat}/K_{m,\,OA} = 12 \times 10^3\ M^{-1}\ s^{-1}$ (G729R E1a) (Table 1); hence, the G729R substitution did not affect carboligation function.

Third, the products and kinetics of their formation were determined for both half-reactions of the oxidative side-reaction in Scheme 1, *lower right-hand quadrant*. In the reductive half-reaction, reduction of molecular O_2 to superoxide/H_2O_2 by G729R E1a and by OADHc assembled with E2o and E3 was evaluated. We hypothesized that the disease-causing G729RE1a substitution that led to a reduced NADH production could affect the superoxide/H_2O_2 production (ROS) by E1a and thereby could contribute to oxidative stress in mitochondria, in accord with findings reported by others (5, 7). The expected primary product is superoxide anion radical generated via one-electron reduction of O_2 with concomitant production in the oxidative half-reaction of the C2(α-hydroxy)-δ-carboxybutylidene–ThDP radical-E1a in Scheme 1 (henceforth called the ThDP-enamine radical) (12, 14, 15). The X-band EPR spectra of the G729R E1a incubated aerobically with OA (10 mM) revealed formation of the ThDP-enamine radical species (Fig. 2*B*). The concentration of ThDP-enamine radical species in the G729R E1a–active centers was estimated as 0.3 μM (0.1% occupancy of active centers). Earlier, similar concentrations of ThDP-enamine radical species were reported for E1a from OA (0.2–0.5 μM (0.1–0.12% occupancy)) (Fig. 2*A*) (12, 14, 15), indicating that this side-reaction was also unaffected by the G729R substitution. The H_2O_2 detected in the reaction assay is a product of dismutation of superoxide radical anion, either spontaneously or by the superoxide dismutase present in the H_2O_2 assay (see Scheme 1, *lower right-hand quadrant*). Again, similar catalytic efficiency of H_2O_2 production resulted by E1a and by G729R E1a by themselves or when assembled into OADHc with E2o and E3: $2.67 \times 10^3\ M^{-1}\ s^{-1}$ (E1a) and $1.47 \times 10^3\ M^{-1}\ s^{-1}$ (G729R E1a) (Fig. 2*C* and Table 1).

It could be concluded that neither the rate of decarboxylation in E1a nor any of the three side-reaction rates of the E1a–ThDP– enamine were significantly affected by the G729R E1a substitution. This suggested that we explore the possibility that assembly of the E1a and E2o components is compromised by the G729R E1a substitution, resulting in reduced overall activity.

G729R E1a substitution does not change the strength of the E1a–E2o interaction

Before turning to kinetic experiments involving both E1a and E2o components, we had to establish whether or not the strength of the E1a·E2o subcomplex was impacted by the G729R E1a substitution. To help identify the loci of, and to determine the strength of interaction between E1a or G729R E1a and E2o, truncated versions of the E2o were created: the $E2o^{1-173}$ di-domain comprising the LDo; the linker region and part of the CDo; and the C-terminal $E2o^{144-386}$ core domain, consisting of the C-terminal part of the linker and the entire CDo (see Fig. 3 for E2o domain assignment). We once again used an approach created at Rutgers to introduce an external *N*-(1-pyrene) maleimide fluorescent label onto the unique Cys^{37} in the $E2o^{1-173}$ di-domain and onto the unique Cys^{178} in the $E2o^{144-386}$ core domain (16). Titration of the pyrene-labeled $E2o^{1-173}$ di-domain and the pyrene-labeled $E2o^{144-386}$ core domain by E1a and by G729R E1a enhanced the pyrene fluorescence intensity, suggesting that a more hydrophobic environment was created around the pyrene fluorophore on their binding (16). The following dissociation constants were calculated: $K_d = 1.12\ \mu$M (E1a) and $K_d = 0.98\ \mu$M (G729R E1a) from titration of the pyrene-labeled $E2o^{1-173}$ di-domain; and $K_d = 3.98\ \mu$M (E1a) and $K_d = 4.79\ \mu$M (G729R E1a) from titration of the pyrene-labeled $E2o^{144-386}$ core domain. These data suggested that E1a binding to the $E2o^{1-173}$ di-domain and to the $E2o^{144-386}$ core domain was not significantly changed by the G729R substitution. In comparison, for E1o, the values of $K_d = 0.041\ \mu$M for the pyrene-labeled $E2o^{1-173}$ di-domain and of $K_d = 0.061\ \mu$M for the pyrene-labeled $E2o^{144-386}$ core domain were reported by us earlier (16), suggesting a different binding mode of E1a and E1o with the same E2o component.

Kinetic evidence for impaired reductive glutarylation of E2o by G729R E1a

The reductive glutarylation of E2o by G729R E1a and OA was studied using a model reaction where E2o was replaced by its LDo ($E2o^{1-87}$) in the reductive glutaryl transfer (see Equation 3 and Scheme 1 (17–19)). On decarboxylation of OA by G729R E1a in the reaction mixture containing LDo, both glutarylated and unglutarylated forms of LDo could be detected by ESI FT–MS at different times of incubation. For G729R E1a, the

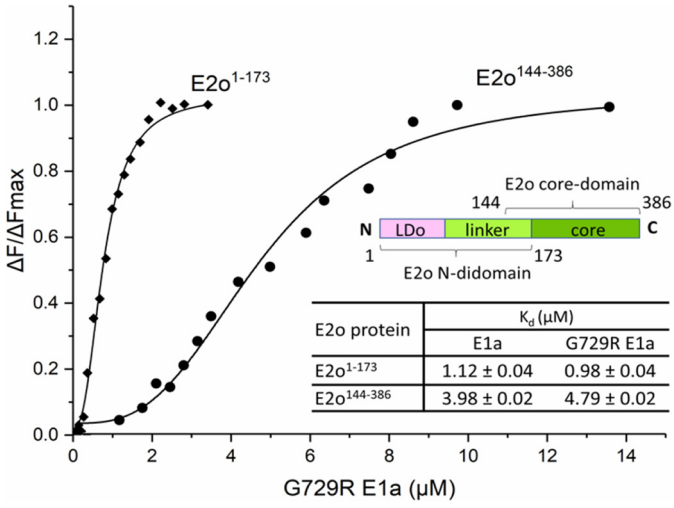

Figure 3. Fluorescence titration curves of pyrene-labeled E2o$^{1-173}$ di-domain and E2o$^{144-386}$ core domain by G729R E1a. *Inset* presents the domain structure of human E2o and K_d values calculated for G729R E1a compared with E1a. Each value represents the mean ± S.D. ($n = 2$).

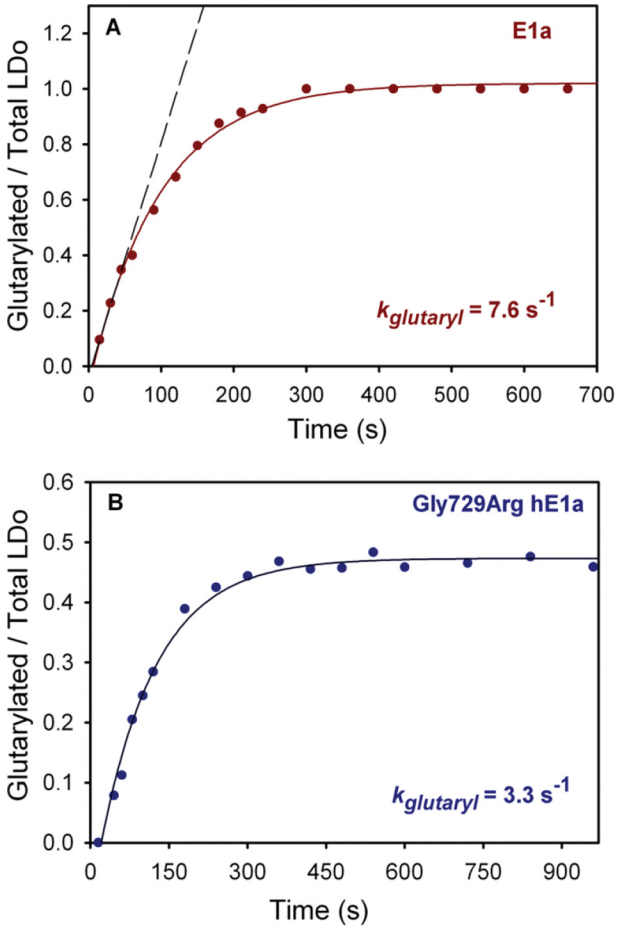

Figure 4. Time dependence for the reductive glutarylation of LDo by E1a or G729R E1a from 2-oxoadipate. *A,* reductive glutarylation of the LDo by E1a and OA. *B,* reductive glutarylation of the LDo by G729R E1a and OA. For both *A* and *B,* LDo (150 μM), E1a or G729R E1a (0.2 μM), and 0.1 mM ThDP in 50 mM NH_4HCO_3 (pH 7.5) were mixed with 2.0 mM OA at 37 °C. Aliquots were withdrawn at time intervals (15–960 s) and were analyzed by FT–MS. The relative intensity of the glutarylated *versus* total LDo (glutarylated + unglutarylated) was plotted *versus* time. The *data points* were fit to single exponential equation ($y = yo + a \times (1 - e^{-kt})$), and the *trace* is a nonlinear regression fit to initial rate conditions. The rate constants were calculated from the initial slope.

fraction of reductively glutarylated LDo *versus* total LDo (glutarylated plus unglutarylated), when plotted against incubation time, enabled calculation of the $k_{glutarylation}$ of 1.8 s^{-1} (at 25 °C) and $k_{glutarylation}$ of 3.3 s^{-1} (at 37 °C) with only 50% of the LDo being glutarylated even after 17 min of the reaction (Fig. 4). When compared with a $k_{glutarylation}$ of 7.6 s^{-1} (at 37 °C) for E1a in the same model reaction, it became evident that there is indeed a reduction in the rate of reductive glutarylation of E2o, but the reduction in the rate could not account for the loss of NADH production by G729R E1a. It should be noted that the calculated values of $K_{m,\ LDo}$ were rather similar for E1a (8.9 μM) and G729R E1a (12 μM). The value was not different from that determined for E1o ($K_{m,\ LDo}$ = 5.4 μM), the established partner of E2o (Fig. S1).

Transthioglutarylation from S8-dihydrolipoyl-E2o to CoA in the E2o core domain forming glutaryl-CoA is significantly impaired by the G729R E1a substitution

The next step in the mechanism after reductive glutarylation of E2o to form *S*8-glutaryl-dihydrolipoyl-E2o (as outlined in Scheme 1) is transfer of the glutaryl group to CoA (Equation 4). A method was developed to measure the rate of enzymatic synthesis of the glutaryl-CoA by MALDI-TOF MS. When measured for E1a and for G729R E1a, both assembled with E2o and E3 into OADHc, a much slower rate was in evidence for G729R E1a (Table 1) (20, 21). At 10 min reaction time, the CoA present in the NADH assay was completely converted to glutaryl-CoA by E1a assembled with E2o and E3. In clear contrast, under the same experimental conditions, including reaction time, with the G729R E1a, both CoA (m/z = 766.414) and glutaryl-CoA (m/z = 880.284) could still be detected in the reaction assay with only ~40% of the CoA converted to glutaryl-CoA (Fig. 5*A* and Fig. S2). The second-order rate constants of k = 0.245 μM^{-1} s^{-1} (E1a) and k = 0.0066 μM^{-1} s^{-1} (G729R E1a) were calculated from the time-dependent kinetic studies (Fig. 5*B*). Apparently, the bulk of the rate reduction in NADH production with the G729R E1a substitution ($k_{cat,\ NADH}$ ~24-fold lower compared with E1a) is the result of the slower rate of glutaryl transfer from the *S*8-glutaryldihydrolipoyl-E2o to CoA ($k_{glutaryl\text{-}CoA}$ ~37-fold lower compared with E1a). This provides clear evidence that the G729R E1a substitution encoded by the pathogenic DHTKD1 mutation affects intermediate channeling, *i.e.* inter-component assembly in the OADHc, because it is the rate of a reaction taking place exclusively on the E2o that is being affected.

HDX–MS reveals different deuterium uptake patterns for E1a and G729R E1a and implies multiple conformations in solution

The results so far summarized suggested that inter-component interactions are impaired by the pathogenic G729R E1a substitution. Before undertaking studies of E1a–E2o interactions, we turned to HDX–MS to study potential conformational changes resulting from the G729R E1a substitution, as may be reflected by changes in deuterium incorporation. On-line digestion of the E1a by pepsin, followed by FT–MS analysis of the resulting peptic peptides, gave evidence for 63 peptides

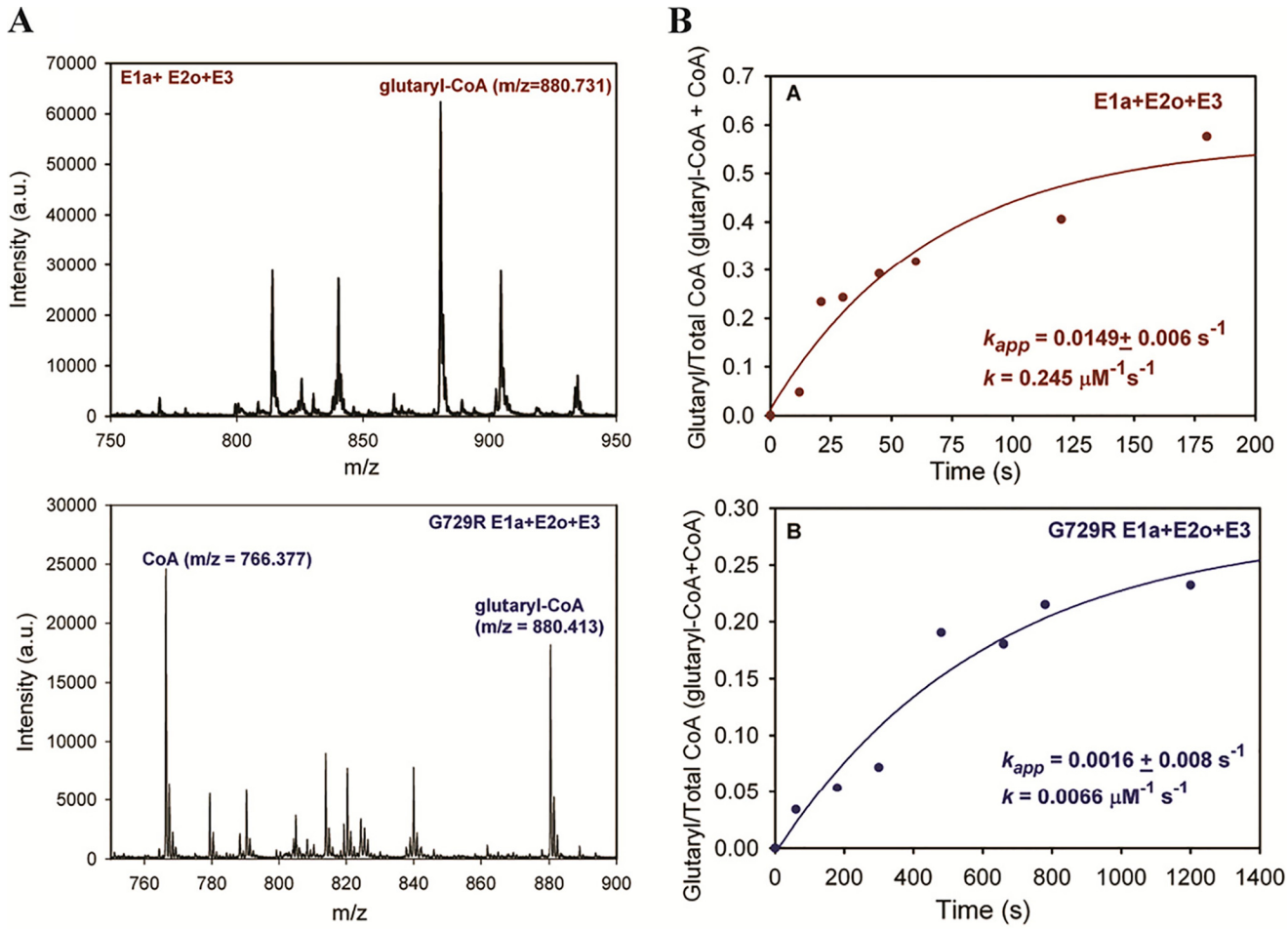

Figure 5. Detection of the glutaryl-CoA product by MALDI-TOF. *A,* MALDI-TOF spectra of CoA and glutaryl-CoA detected in the reaction assay with E1a or G729R E1a assembled to OADHc. The CoA (m/z = 766.414) and glutaryl-CoA (m/z = 880.284) were used as external standards. *B,* time dependence of the fraction of glutaryl-CoA formed. The E1a (0.005 mg) or G729R E1a (0.020 mg) was assembled with E2o and E3 at a mass ratio of E1a/E2o/E3 (mg/mg/mg) = 1:2:5 and incubated for different times in the reaction assay containing all components necessary for the overall OADHc assay, OA (2.5 mM), and CoA (300 μM). The fraction of glutaryl-CoA *versus* total CoA (CoA plus glutaryl-CoA) estimated based on the relative peak heights intensities was plotted against time of incubation and enabled calculation of k_{app} of glutaryl-CoA formation and the second-order rate constants. The data points were fit to single exponential equation ($y = yo + a \times (1 - e^{-kt})$), and the line is the regression fit trace. The values of k_{app} ± standard errors are presented.

(Table S1) with many of them partially overlapping and providing 90% sequence coverage for E1a. Similar peptides resulted on pepsin digestion of the G729R E1a according to FT–MS analysis (data not shown). A brief interpretation of the results is merited in view of the large amount of information content. In Fig. 6, there are two types of plots. In Fig. 6*A*, they are presented as "mirror"' images of pepsinolytic peptides of E1a and G729R E1a with the sequence assignment on the *x* axis and time course of intensity change on the *y* axis as Δ*D* values (%). Although the results appear to create continuous curves, in fact, each *x* value represents a distinct pepsinolytic peptide. The true power of the method and of the results is most pronounced in the difference plot (Fig. 6*B*), where corresponding values for E1a are subtracted from those for G729R E1a, producing a ΔΔ*D* intensity difference on the *y* axis (in Da units). The comparative HDX–MS analysis of the E1a and G729R E1a presented in Fig. 6*A* indicates that peptides with high levels of deuteration are mostly located in three regions: in the N-terminal region (peptides encompassing residues 16–20, 24–47, and 83–92); in the ThDP- and Mg^{2+}-binding region (231–271, 363–381, 401–421,485–530, 506–518, and 536–546); and in the C-terminal region (769–778 and 888–901) (see Fig. S3 for percent deuterium incorporation of E1a and G729R E1a mapped onto the modeled structure of E1a). The difference HDX–MS plot presented in Fig. 6*B* indicates that whereas the G729R E1a substitution did not induce large-scale conformational changes, local backbone amide proton perturbations were indeed observed. A positive ΔΔ*D* in the difference plot implies that some peptides in the G729R E1a are more open to deuterium uptake compared with E1a, whereas a negative ΔΔ*D* suggests that some peptides in the E1a are more open to deuterium uptake than the G729RE1a. For example, peptides comprising residues ^{24}YQTERGVYGYRPRKPESREPQGAL^{47} in the N-terminal region and residues ^{401}SPEEVVRATRLAFEYQRQFRK^{421} near the ThDP- and Mg^{2+}-binding region of G729R E1a displayed an obvious decrease in deuterium incorporation, indicating that those regions are likely less open to the deuterium uptake. In Fig. 6*C*, peptides that become less open for deuterium uptake on the G729RE1a substitution are color-coded in *blue* on the modeled E1a structure, whereas peptides more open for deuterium uptake are color-coded in *red*. The data reveal obvious changes in deuterium uptake on G729R E1a substitution. Also,

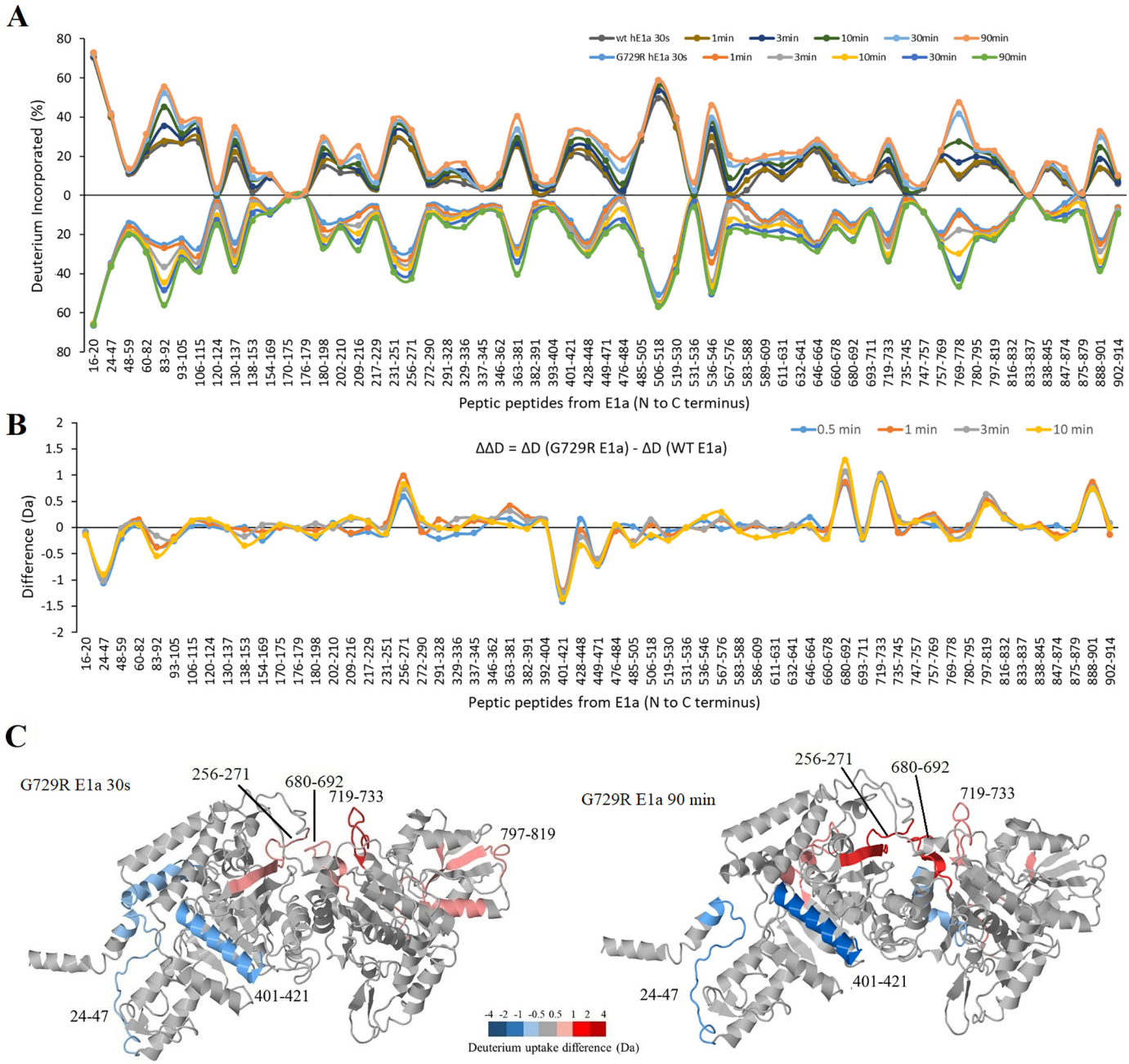

Figure 6. Comparative HDX–MS analysis of the peptic peptides from E1a and from G729R E1a. *A,* butterfly plot representing relative deuterium incorporation percentage (Δ*D*%, *y* axis) deuterons exchanged/maximum exchangeable amides × 100% of peptic peptides from E1a (*top*) and from G729R E1a (*bottom*) (*x* axis, listed peptic peptides from the N to C terminus). *B,* difference HDX–MS plot showing the changes in deuterium incorporation (Δ*ΔD*, *y* axis) (deuterons exchanged in G729R E1a minus deuterons exchanged in E1a) of peptic peptides from E1a (*x* axis, listed peptic peptides from the N to C terminus). *C,* G729R E1a monomer structure is colored according to the deuterium uptake difference at the first (30 s) and last (90 min) time points. (The E1a structure was built based on a homology model of *Ms*KGD (PDB code 2XT6 (25) using I-TASSER server (47)).

deuterium uptake by the peptide comprising residues 401–421 in G729R E1a was reduced by 1.4 Da at 10 min of exchange, and even after 90 min of exchange, a 2.3 Da mass reduction still persisted (see Fig. 7 for deuterium uptake difference plot). The residue Lys[37] in peptide 24–47 was identified as a "hot spot"–linking site by CL–MS (see under "Chemical cross-linking of E1a or G729R E1a with E2o identifies different inter-component interaction loci"), suggesting regional conformational change in this region that perhaps impacts the interaction of E1a and E2o. In contrast, an increase in deuterium uptake was observed in the peptide [256]SATGDVLSHLTSSVDL[271] in G729R E1a suggesting that it is more open to deuterium exchange compared with E1a (Fig. 7). Importantly, peptides from the C-terminal region of G729R E1a comprising residues [680]ISGGEAKWLLQSG[692], [719]MCDSAEEGVDGDTVN[733] (including the substitution site at G729), [797]VDPKKVKTLVFCSGKHFYSLVKQ[819], and [888]RLVGRPPLPVPAVG[901], experienced a significant increase in deuterium uptake level compared with E1a, suggesting more accessibility to the deuterium in response to the G729R E1a substitution (Fig. 7, *bottom panels*). These findings clearly signal conformational changes induced by the G729R E1a substitution.

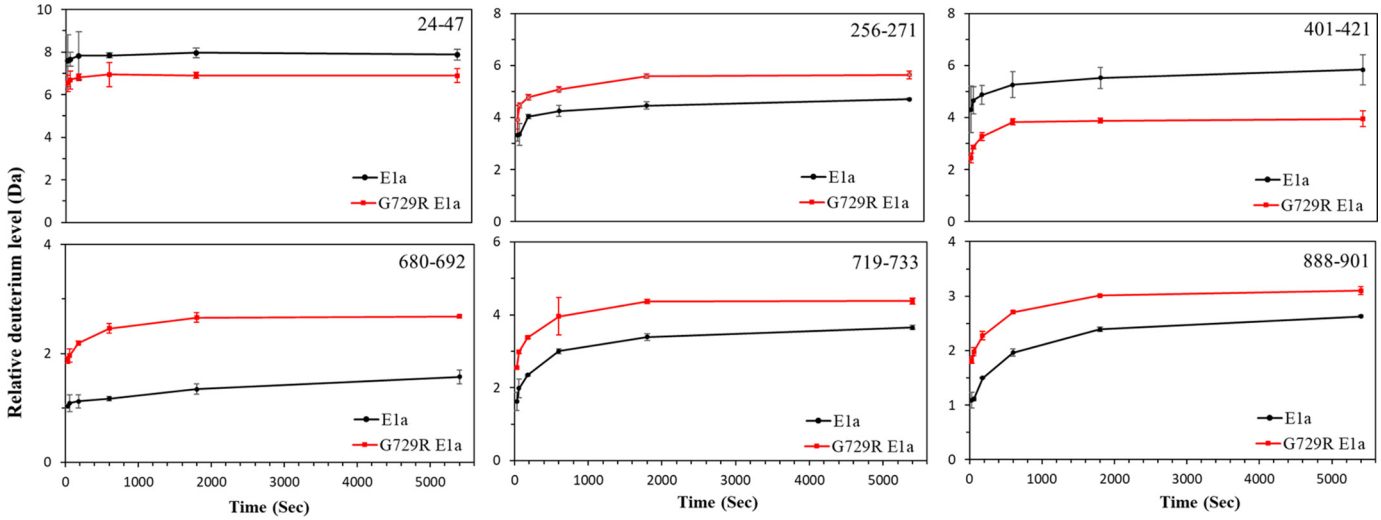

Figure 7. Deuterium uptake difference plot for peptic peptides originated from E1a and G729R E1a. The presented peptic peptides are encompassing residues from the N-terminal region (residues 24–47), ThDP–Mg^{2+}-binding region (residues 256–271; 401–421) and C-terminal region (residues 680–692, 719–733, and 888–901) for both E1a (*black*) and G729R E1a (*red*). The deuterium uptake levels were plotted by using the mean value of two independent experiments with errors representing the S.D.

Observation of EX1 HDX kinetic behavior further supports two solution conformations of E1a

A closer examination of the high-resolution MS signals revealed several peptides with bimodal mass envelope distributions that could be curve-resolved into two closely-spaced peaks, an indication of "EX1 kinetics" (22). Unlike those peptides behaving according to "EX2 kinetics," characterized by mass peaks gradually shifting to higher mass in MS-based analysis with peaks moving to the right, the spectrum of "EX1 peptides" displayed two populations: a higher m/z envelope, which has undergone an unfolding event (to the right), and a lower m/z envelope, which has not (to the left in the deconvoluted spectrum) (23, 24). Among the "EX1 peptides" identified in this study are peptides encompassing residues 256–271, 680–692, and 797–819 (see time course of HDX for the three peptides with side-by-side presentation of deconvoluted spectra for E1a and G729R E1a in Fig. 8*A*). Occurrence of EX1 kinetics provides a direct measure of a conformational transition. These findings indicate that there likely are at least two conformations of E1a under physiological conditions, in accord with the interpretation of the difference mass spectrum in Fig. 6*B*. In each of these peptides, the G729R E1a substitution results in a shift to a more open conformation in these regions (more deuterium absorbed in the "open" conformation), which could compromise the formation of a catalytically-competent E1a conformation required for productive interaction between the E1a and E2o components in OADHc.

Where the quality of the data allowed, the first-order rate constant could be estimated for the conformational interconversion by fitting the change in the relative abundance to a simple rate expression $\ln([A]/[A]_0) = -kt$, which in turn led to the half-time of unfolding ($t_{½} = \ln 2/k$). As an example, for peptide 256–271 at 0.5 min, 20% in E1a and 47% of G729R E1a have undergone an unfolding event, respectively. This corresponds to a 3-fold decrease in the $t_{½}$ of unfolding of G729R E1a (3.4 min) compared with E1a (10 min).

These findings could also be placed in a broader context. Excellent X-ray crystallographic studies reported for the related *Mycobacterium smegmatis* 2-ketoglutarate decarboxylase (*Ms*KGD (25, 26)) have already alluded to multiple conformations of some of the peptides reported here, as indicated by the sequence alignment for selected peptides (see Fig. 8, *B* and *C*). For example, the peptide comprising residues 256–271 is part of the E1a amino acid sequence, which on alignment with *Ms*KGD corresponds to the *Ms*KGD active center loop comprising residues 560–580 (26). It was suggested that this flexible loop adopts at least three distinct conformations: an opened state that shows conformational disorder in the available crystal structures to allow the substrate to enter the active site; a closed "lid" conformation that sequesters the active site to isolate the Michaelis complex or the post-decarboxylation intermediate; and an outer conformation that creates a tunnel for incoming substrate acceptor (26).

HDX–MS of E1a or G729R E1a with E2o present

To address the question as to which site on E1a interacts with which site on E2o, and whether these loci could be changed by the G729R E1a substitution, we carried out HDX–MS analysis by comparing the deuterium uptake of the peptic peptides that originated from E1a and G729R E1a in the absence and in the presence of E2o (Fig. 9). For a complete set of deuterium uptake curves for peptic peptides originating from E1a, G729R E1a, and the E1a·E2o and G729R E1a·E2o subcomplexes, see Fig. S4. The major findings are as follows.

(i) The HDX–MS experiments indicate that the interaction of E1a with E2o did not induce large-scale conformational changes in E1a; however, local backbone amide proton perturbations were indeed observed.

(ii) In contrast to the evidence for the E1a–E2o interaction, the HDX–MS data provide no clear evidence for major changes in deuterium uptake upon binding of G729R E1a to E2o at any H/D exchange time points analyzed, suggesting only a transient

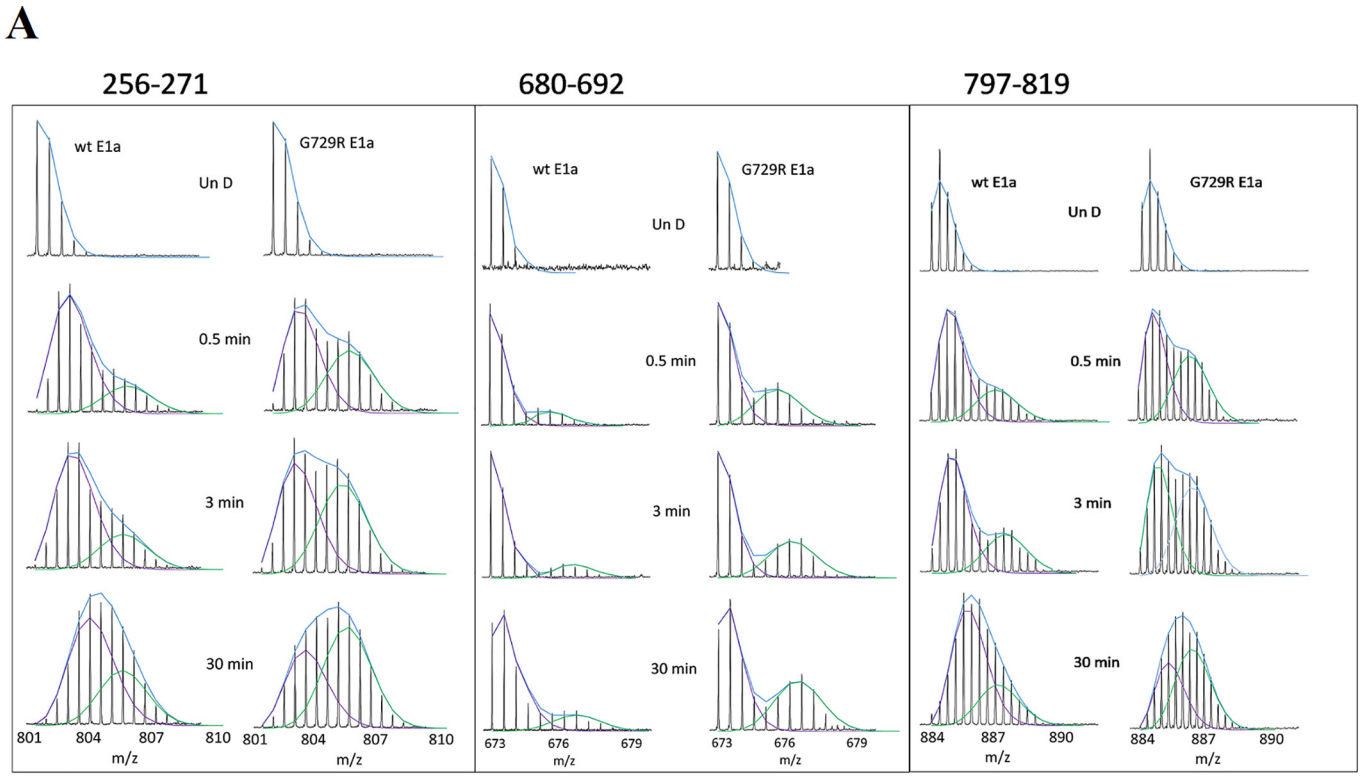

Figure 8. Peptides displaying EX1 kinetics in E1a and G729R E1a. *A,* bimodal isotopic distribution for selected peptides at 0, 0.5, 3, and 30 min of H/D exchange; lower *m/z* population is shown in *purple,* and higher *m/z* population is shown in *green*. *B,* position of peptides that displayed EX1 kinetics in the E1a monomer structure in different orientations. The Gly^{729} position is indicated in *green*. The position of the peptides encompassing residues 256–271 (*red*), 680–692 (*yellow*), and 797–819 (*pink*) is indicated. *C,* high conservation of the E1a amino acid sequences encompassing residues 256–271, 680–692, and 797–819 with *Ms*KGD. The active center loop encompassing residues 560–580 in *Ms*KGD adopts at least three distinct conformations (26).

interaction between the two components that could be too weak to be captured by the method used (Fig. 9*B* and Fig. S4).

(iii) Importantly, as shown in Fig. 9, *A* and *C*, the region from the N-terminal end of E1a comprising residues 24–47 experienced significant protection from deuterium uptake in the subcomplex with E2o, similar to E1o (corresponding to the region comprising residues 27–40) (16). Another region that experienced significant protection from deuterium uptake on compl-

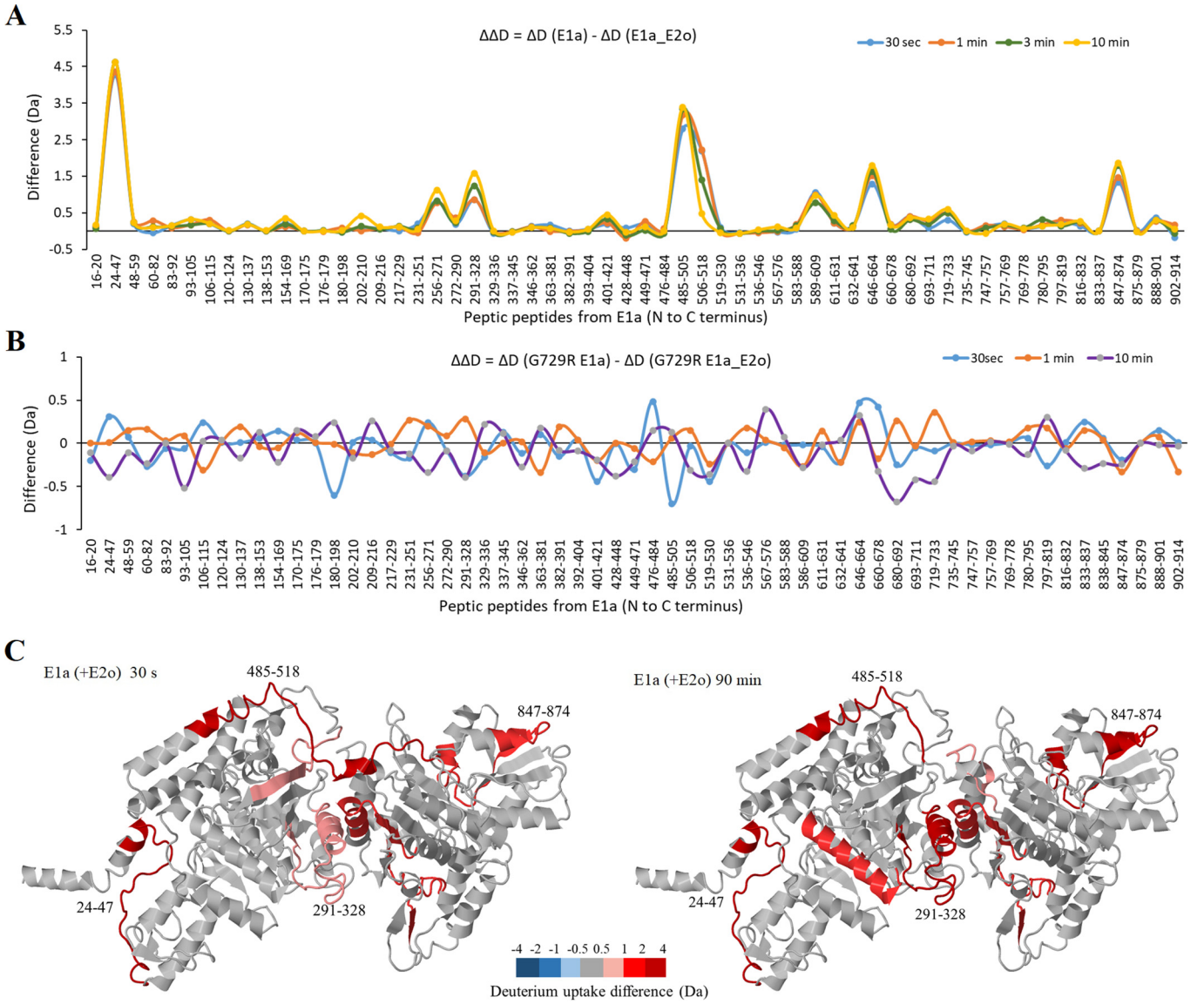

Figure 9. Comparative HDX–MS analysis of the E1a and G729R E1a by itself and on interaction with E2o. Difference plot showing the changes in deuterium incorporation of peptic fragments of E1a (*A*) and G729R E1a (*B*) in the absence and presence of E2o (ΔΔ*D*, *y* axis) (deuterons exchanged in the absence and presence of E2o). *C*, E1a peptides highly protected from H/D exchange on interaction with E2o are color-coded according to the deuterium uptake difference at the first (30 s) and last (90 min) time point.

exation with E2o comprises residues 485–518, which according to a recently reported X-ray structure of human E1a is part of the novel extended linker region (residues 497–527) connecting two halves of the E1a monomer (27) (PDB number is not available yet). In the C-terminal region, the peptides comprising residues 589–609, 646–664, and 847–874 also experienced protection from deuterium uptake on interaction with E2o.

Chemical cross-linking of E1a or G729R E1a with E2o identifies different inter-component interaction loci

We next carried out chemical CL–MS in binary E1a·E2o and G729R E1a·E2o subcomplexes (16). The motivation to establish the loci of interaction in the binary subcomplexes was that neither the reported X-ray structures of the core domain of the E2s (28–30) nor the 7-Å resolution X-ray structure of the full-length mammalian E2o provided information regarding the lipoyl domain and subunit-binding region (31), presumed to interact with the E1 and E3 components. Also, there is not an X-ray structure for any of the 2-oxo acid dehydrogenase complexes due to their size (M_r of 4–10 million) and the flexible and distant attachment of the E1 and E3 components to the E2 core (32–35).

An MS-cleavable zero-length cross-linker (1,1′-carbonyldiimidazole (CDI) with a spacer length of 2.6 Å and Cα–Cα distance of ~16 Å to be bridged) (36) was employed to react with the ϵ-amino side chain of the lysine residues of the full-length E1a or G729R E1a in subcomplex with E2o. Two types of cross-linked peptides were identified: (i) intra-component cross-links, *i.e.* two lysines within the same subunit or between two identical subunits being cross-linked (recall that E1a is a dimer, whereas E2o is probably a trimer), and (ii) the inter-component cross-links, where cross-linking between the E1a and E2o components takes place at a max-

Table 2
Unique intra-component (both intra-subunit and inter-subunit) cross links identified in E1a and in G729R E1a with CDI cross-linker

Unique intra-component cross links in E1a		Cross-linked Lys		Merox
Peptide 1[a]	Peptide 2[a]	site 1	site 2	score
^{70}AAK^{72}	^{684}EAK^{686}	Lys^{72}	Lys^{686}	122
^{143}KDWFAK^{148}	^{539}VEVPRELQMHSHLLK^{553}	Lys^{148}	Lys^{553}	73
^{153}LQK^{155}	^{879}FEKEL^{883}	Lys^{155}	Lys^{881}	61
^{244}KMR^{246}	^{438}LDEPFYTNPIMYKIIR^{453}	Lys^{244}	Lys^{450}	60
^{244}KMR^{246}	^{456}KSIPDTYAE^{464}	Lys^{244}	Lys^{456}	112
^{421}KDVIIDLLBYR^{431}	^{533}FVGMKSVEVP^{543}	Lys^{421}	Lys^{537}	98
^{563}MmDGIKLDWATAE^{575}	^{759}KPLIVASPK^{767}	Lys^{568}	Lys^{759}	94
^{850}mSKYK^{854}	^{881}KQLABK^{886}	Lys$^{852/854}$	Lys^{881}	71
Unique intra-component cross links in G729R E1a				
Peptide 1	Peptide 2			
^{244}KMR^{246}	^{759}KPLIVASPK^{767}	Lys^{244}	Lys^{759}	77
^{292}AVNPVAVGKTR^{302}	^{533}FVGMKSVEVPR^{544}	Lys^{300}	Lys^{537}	122
^{292}AVNPVAVGKTR^{302}	^{613}TDDTYIPLNHMDPNQKGFLE^{632}	Lys^{300}	Lys^{628}	120
^{300}KTR^{302}	^{784}PGTTFNPVIGDSSVDPKK^{801}	Lys^{300}	Lys$^{800/801}$	72
^{438}LDEPFYTNPIMYK^{450}	^{787}TFDPVIGDSSVDPKK^{801}	Lys^{450}	Lys$^{800/801}$	47
^{456}KSIPDTYAE^{464}	^{563}MMDGIKLDWATAE^{575}	Lys^{456}	Lys^{568}	118
^{762}IVASPK^{767}	^{852}KYKHVK^{857}	Lys^{767}	Lys$^{852/854}$	45

[a] m indicates oxidized Met; B indicates *S*-acetamido-Cys; also consider the common deamination of Asn to Asp and Gln to Glu (from N to D and from Q to E); cross-links were evaluated using software tool Merox 1.6.6 (46).

imal distance determined by the length of the spacer (Fig. S5) (37).

(i) The comparison of the CL–MS data revealed numerous intra-component cross-links for both E1a (85 cross-links) and for G729R E1a (87 cross-links) (Tables S2 and S3). The most frequently identified intra-component cross-links were between E1a residues located in the N-terminal region (Lys^{37}, Lys^{72}, Lys^{148}, and Lys^{155}), residues in the ThDP- and Mg^{2+}-binding region (Lys^{300}, Lys^{450}, and Lys^{456}), and those located in the C-terminal region (Lys^{767}, Lys^{818}, Lys^{826}, Lys^{827}, and Lys$^{852/854}$) that could reflect a spatial proximity of these regions in the E1a dimer assembly. However, there were also some unique intra-component cross-links identified that are specific for E1a or for G729R E1a only (Table 2). Thus, Lys^{244} in E1a forms unique cross-links with Lys^{450} and Lys^{456} from the ThDP- and Mg^{2+}-binding region, whereas in G729R E1a, the Lys^{244} forms a unique cross-link with Lys^{759} from the C-terminal region (Table 2). Also, in G729R E1a, the Lys^{300} from the ThDP- and Mg^{2+}-binding region forms other cross-links with residues Lys^{537}, Lys^{628}, and Lys$^{800/801}$, which are not detected in E1a. The data suggest that the G729R E1a substitution could induce regional conformational changes of E1a, in agreement with the HDX–MS data presented above, thus likely affecting its interaction with the E2o component.

(ii) On interaction of E1a or G729R E1a with the E2o component, multiple inter-component cross-links were identified for the first-time: 63 cross-linked residue pairs were identified for the E1a·E2o subcomplex (Table S4) and 66 for the G729R E1a·E2o subcomplex (Table S5). The MS dataset related to Tables S1–S5 has been deposited to the Proteome Xchange Cosortium via PRIDE (PXD017792). In summary, the following cross-linked Lys residues were identified on both E1a and G729R E1a: Lys^{148} and Lys^{188} from the N-terminal region; Lys^{300} and Lys^{450} from the ThDP- and Mg^{2+}-binding region; and Lys^{818}, Lys$^{826/827}$, and Lys$^{852/854}$ from the C-terminal region. On E2o, the cross-linked Lys^{24}, Lys^{43}, Lys^{66}, Lys^{78}, and Lys^{87} are from the lipoyl domain; Lys^{150} and Lys^{159} are from the linker region of E2o; and Lys^{240}, Lys^{286}, Lys^{289}, Lys^{342}, Lys^{371}, and Lys^{373} are from the E2o core domain (Tables S4 and S5). Intriguingly, a great number of cross-links formed between the Lys residues from the C-terminal region of E1a and of G729R E1a and those from the lipoyl domain of E2o have been detected, suggesting that the C-terminal region of E1a/G729R E1a could be important for interaction with E2o and for substrate channeling. Almost half of the cross-linked Lys residues in E2o are located within its catalytic/core domain, where the glutaryl group is transferred from *S*-glutaryldihydrolipoyl-E2o to CoA with the formation of glutaryl-CoA in Equation 4, whereas Lys^{98}, Lys^{150}, and Lys^{159} from the linker region could be considered as "hot spot" lysines (*i.e.* participate in multiple cross-links) for the E1a–E2o interaction.

Additionally, some unique inter-component cross-links were identified for the E1a·E2o and G729R E1a·E2o subcomplexes (Fig. 10*A*, where the meridian represents the E2o component with its three domains: lipoyl domain, linker region, and core domain), suggesting that local conformational changes induced by the G729R substitution could lead to different cross-links. In the G729R E1a·E2o subcomplex, the Lys^{818} from the C-terminal E1a region forms a few unique cross-links with Lys^{78} from the lipoyl domain of E2o, and with Lys^{240} and Lys^{342}, both from the E2o core. In the E1a·E2o subcomplex only two unique cross-links were identified: Lys^{69} from the N-terminal region of E1a forms a cross-link with Lys^{172} from the E2o linker region, and Lys^{886} from the C-terminal region of E1a forms a cross-link with Lys^{342} from the E2o core domain (see Fig. 10*B* where lysine residues involved in unique inter-component cross-links in E1a and in G729R E1a are mapped onto the structure of E1a). HDX–MS and chemical cross-linking data both provide evidence for local conformational changes in the C-terminal region of E1a that could affect E1a–E2o interaction and intermediate channeling. Although none of the three side-reactions of the E1a–ThDP–enamine intermediate are affected, the glutaryl group's channeling through the OADHc and formation of the glutaryl-CoA product are significantly impaired by the G729R E1a substitution (see Figs. S7–S10 where all MS/MS spectra for cross-links identified in E1a, G729R E1a, E1a·E2o subcomplex, and G729RE1a·E2o subcomplex are presented).

Conclusions

Data presented in this paper provide the first evidence that a heterozygous missense mutation (c.2185G→A (p.Gly729Arg)) identified in the *DHTKD1* gene encoding E1a and linked to pathogenesis of AMOXAD is associated with impairment of OADHc function. Sequence alignment of all known *DHTKD1*-encoded proteins (E1a's) and human E1o revealed that the C-terminal region is highly conserved among the DHTKD1 species (and in E1o); however, the Gly^{729} residue is unique for E1a species but is not present in human E1o or in human E1o-like protein (Fig. S6).

Biochemical studies compared the behavior of G729R E1a to E1a itself, both as isolated components and when assembled to OADHc. Tracing the reactions along the path in Scheme 1, they conveniently fall into two categories, those pertinent to E1a by itself and those requiring the E2o (second) and even E3 (third) component of OADHc. The rates of neither the decarboxylation of OA nor of the three side-reactions emanating from the enamine intermediate were significantly affected by the G729R

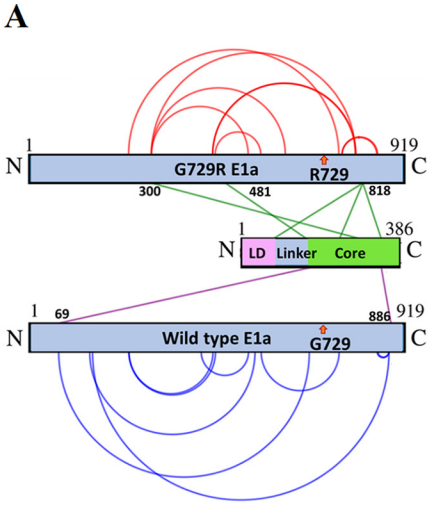

Peptide from hE1a	Peptide from hE2o	Cross-linked lysine site		Merox score
		site 1	site 2	
Unique inter-component cross links in E1a-E2o				
^{65}EHGHK^{69}	^{171}LKE^{173}	Lysine^{69}	Lysine^{172}	72
^{886}KLR^{888}	^{329}MHGIFDRPVAIGGK^{342}	Lysine^{886}	Lysine^{342}	100
Unique inter-component cross links in G729R E1a-E2o				
^{292}AVNPVAVGKTR^{302}	^{289}KNE^{291}	Lysine^{300}	Lysine^{289}	128
^{480}IKSSYYAK^{487}	^{156}HREK^{159}	Lysine^{481}	Lysine^{159}	117
^{817}VKER ^{820}	^{78}KTGAA^{82}	Lysine^{818}	Lysine^{78}	64
^{817}VKQRE^{821}	^{234}VIDDTTKE^{241}	Lysine^{818}	Lysine^{240}	103
^{816} LVK^{818}	^{328}GMHGIFDRPVAIGGK^{342}	Lysine^{818}	Lysine^{342}	112

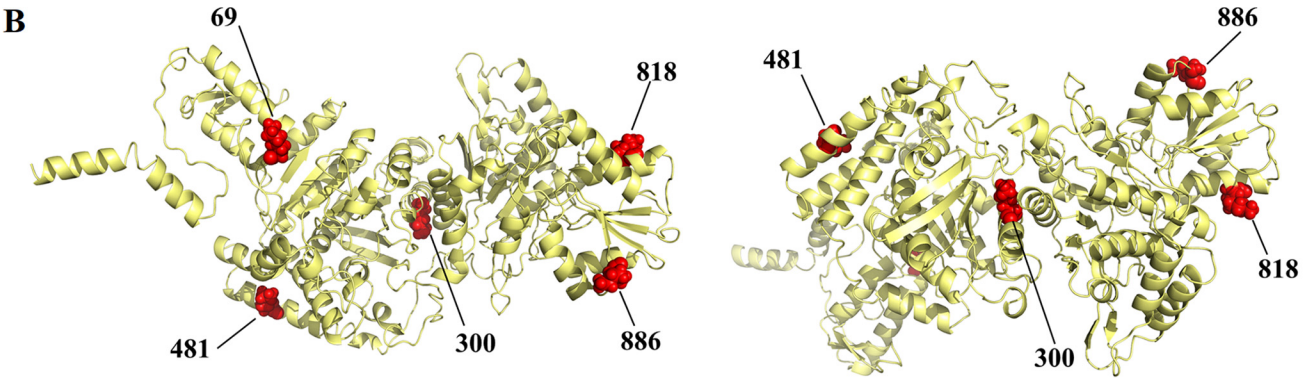

Figure 10. Chemical cross-linking of E1a and G729R E1a in subcomplex with full-length E2o by CDI cross-linker. *A, left,* schematic representation of the intra-component and inter-component unique cross-links identified for E1a and for G729R E1a by themselves and on their interaction with E2o. *A, right,* unique inter-component cross-links identified on interaction of E1a and G729R E1a with E2o by CDI. Cross-links were evaluated using the software tool Merox 1.6.6 (46). *B,* lysine residues from the unique cross-links formed by E1a (Lys^{69} and Lys^{886}) and by G729R E1a (Lys^{300}, Lys^{481}, and Lys^{818}) on interaction with E2o are mapped onto the E1a structure in two different orientations.

substitution, perhaps not surprising in view of the distant location of the site of substitution from the ThDP–Mg^{2+} active center. The three subsequent reactions, (i) reductive glutarylation of E2o by E1a and OA, (ii) glutaryl transfer from *S*8-glutaryldihydrolipoyl-E2o to CoA producing glutaryl-CoA (a reaction whose mechanism of transthiolesterification we had examined recently (38)), and (iii) NADH production as a measure of the rate of the overall reaction of the complex, were indeed measurably reduced, well beyond experimental error. The specific measurement especially of glutaryl-CoA formation rates clearly implied that interaction between the E1a and E2o was compromised by the G729R E1a substitution, leading to the reduced overall NADH activity and suggesting the mass spectrometric experiments to identify any structural impact of the substitution.

HDX–MS, specifically the difference spectrum in Fig. 6*B*, provides strong evidence that the G729R E1a has several regions displaying different H/D exchange uptake and suggesting that there is measurable conformational change accompanying the G729R substitution.

Identification of peptic peptides reporting an EX1 kinetic behavior for HDX gave further evidence for the presence of at least two solution conformations of the E1a and showed how the single G729R E1a substitution could shift the conformational equilibrium to a more open one.

The HDX–MS experiments indicate that the interaction of E1a with E2o did not induce large-scale conformational changes in E1a; however, local backbone amide proton perturbations were indeed observed in the N-terminal region, the ThDP- and Mg^{2+}-binding fold, and in the C-terminal region in Fig. 9. In contrast to the evidence for E1a–E2o interaction, the HDX–MS data provide no clear evidence for major changes in deuterium uptake upon binding of G729R E1a to E2o at any H/D exchange time points analyzed, suggesting only a transient interaction between the two components that could be too weak to be captured by the method used.

The HDX–MS experiments were followed by CL–MS experiments using a zero-length cross-linker to identify potential differences in the loci of E1a–E2o interactions resulting from the G729R E1a substitution. Among the unique differences in the cross-linking map in Fig. 10, it is notable that Lys^{886} of E1a, but Lys^{818} of G729R E1a, interacts with the core Lys^{342} of E2o, once more confirming conformational changes with the substitution. Given that Lys^{342} is proximal to the active center of the E2o core domain (38, 39) responsible for glutaryl-CoA formation, this change could diminish the rate of glutaryl-CoA for-

mation detected by kinetics. Additional interaction of note is Lys^{818} of G729R E1a cross-linked to Lys^{78} of E2o of the lipoyl domain. This cross-link could also contribute to the lower rate observed.

The functional and structural studies presented herein provide insight into the molecular basis of the c.2185G→A (p.G729R)) pathogenic mutation in *DHTKD1* that impaired the function of the OADHc in the L-lysine metabolic pathway. On the basis of our MS findings, a simple explanation of the reduced activity of the G729R E1a variant is steric interference originating from the additional E1a–E2o interactions, partly blocking the lipoylation site and the active center of E2o. We also note, however, that the reduction in the rate of NADH produced by a factor of 40–50 by the G729R E1a substitution, rather small in energetic terms, is probably the result of a number of contributions.

Having here identified the step in the complex mechanism that is responsible for the slower rate in NADH production, as well as the likely loci where the "misalignment" of the interaction of substituted E1a and E2o originates, the challenge here created is to the medicinal chemist to design agents to counteract the consequence of the pathogenic mutation.

Experimental procedures

Protein expression and purification

Expression and purification of human E1o, E1a, E2o, and E3 was as reported by us earlier (10). For construction of plasmid, expression, and purification of E2o-derived proteins, the pET-15b-E2o plasmid encoding the N-terminal His_6-tag E2o was used as template, and the amplification primers and their complements were used for site-directed mutagenesis to introduce a TAA stop codon in place of Lys^{88} and Glu^{174} (the numbers include Met as the first amino acid). The following E2o-derived proteins were created: $E2o^{1-87}$ (LDo, comprising lipoyl domain and partially a linker region) and $E2o^{1-173}$ di-domain (comprising LDo and linker region (10)). The gene encoding C-terminally truncated His_6-tagged $E2o^{144-386}$ core domain was synthesized by ATUM (Newark, CA).

Construction of plasmid, expression, and purification of G729R E1a

The gene encoding the C-terminal His_6-tagged E1a was synthesized by ATUM. The *DHTKD1* gene was codon-optimized for expression in *Escherichia coli* cells and was inserted into pET-22b(+) through the NdeI and XhoI restriction sites, and the resulting plasmid was expressed in BL21(DE3) cells. Cells were grown in LB medium supplemented with 50 μg/ml ampicillin containing 1 mM $MgCl_2$ and 0.50 mM thiamin-HCl. Protein expression was induced by 0.5 mM isopropyl 1-thio-β-D-galactopyranoside for 15 h at 18 °C (10). The G729R E1a variant was created by using QuikChange II XL site-directed mutagenesis kit. The following amplification primer containing the desired G279R mutation and its complement were used for the mutagenesis reaction: 5′-GCTGAGGAGGGTGTTGACCGTGATACGGTTAACATGTTTG-3′ and 5′-CAAACATGTTAACCGTATCACGGTCAACACCCTCCTCAGC-3′.

The DNA substitution was confirmed by sequencing at GENEWIZ, LLC (South Plainfield, NJ). The G729R E1a displayed good expression and was purified to homogeneity by using Ni-Sepharose high-performance affinity media.

Activities of the E1a and of OADHc in different assay systems

(i) Overall and E1a-specific activities were measured as reported by us earlier (10, 11, 14).

(ii) Formation of glutaric semialdehyde by E1a and by G729R E1a was measured in an alcohol dehydrogenase-coupled reaction assay containing: 0.1 M Tris·HCl (pH 7.5), 150 mM NaCl, 0.5 mM ThDP, 2.0 mM $MgCl_2$, 0.25 mM NADH, 1 mM DTT, 1% glycerol, 0.08 mg/ml horse liver alcohol dehydrogenase (ADH), and 1.0 mM OA. Reaction was initiated by E1a or by G729R E1a (0.10 mg/ml) after 1 min of equilibration at 37 °C. The rate of NADH oxidation was measured at 340 nm from the initial slope of the recorded progress curve.

(iii) The rate of H_2O_2 production by E1a and G729R E1a and by assembled OADHc was measured using a fluorescent Amplex UltraRed reagent as was reported by us recently for E1o and for OGDHc (11).

(iv) CD spectroscopy was used for the detection of the (*S*)-2-hydroxy-3-oxoheptanedioic acid, a carboligation product formed in the reaction of the E1a–ThDP–enamine intermediate with glyoxylate as an acceptor as reported by us earlier (11, 14).

(v) Reductive glutarylation of the E2o lipoyl domain by E1a and by G729R E1a was by FT–MS as reported by us earlier (11, 17, 38).

Enzymatic synthesis of glutaryl-CoA

For the enzymatic synthesis of glutaryl-CoA, the E1a (0.15 mg) or G729R E1a (0.15 mg) was assembled with E2o (0.30 mg) and E3 (0.75 mg) into OADHc in 0.15 ml of 0.1 M Tris·HCl (pH 7.5) containing 0.3 M NH_4Cl, 0.5 mM ThDP, and 2.0 mM $MgCl_2$ at 25 °C. The mass ratio of the E1a/E2o/E3 components of 1:2:5 (mg/mg/mg) was selected from an optimization of the overall NADH assay. After 40 min of incubation, an aliquot containing 0.005 mg of E1a or 0.020 mg of G729R E1a was withdrawn and was placed into 0.4 ml of the reaction assay containing all components necessary for the overall NADH assay. The reaction was initiated by addition of OA (2.5 mM) and CoA (300 μM) after 1 min of equilibration at 37 °C in a Thermomixer (Eppendorf). The reaction was terminated at different times by acidification on addition of 2.5% TFA to a final concentration of 0.1%, and samples were kept at 4 °C. The glutaryl-CoA formed in the reaction was purified according to the protocol reported (21). The samples were analyzed with a 355-nm laser in a negative mode on the ultrafleXtreme MALDI spectrometer (Bruker Daltonics, Bremen, Germany). For each spectrum, five subspectra with 400 laser shots with 400 Hz frequency were acquired. The spectra were analyzed using flexAnalysis 3.0 software (Bruker Daltonics, Bremen, Germany) and were smoothed using the Savitzky-Golay algorithm after baseline subtraction.

Electron paramagnetic resonance spectroscopy

The sample preparation and EPR experiment for detection of ThDP–E1a- and G729R E1a-bound radical species was as reported by us earlier (11, 14, 15).

Fluorescence spectroscopy

All fluorescence spectra were recorded at 25 °C by using a Varian Cary Eclipse fluorescence spectrophotometer. Titration experiments were conducted in 100 mM HEPES (pH 7.5), containing 0.15 M NaCl and 1% glycerol. The $E2o^{1-173}$ di-domain and $E2o^{144-386}$ core domain (50 μM), each containing a single cysteine residue at positions 38 and 179, respectively, were labeled with *N*-(1-pyrene) maleimide according to a protocol reported by us earlier (16). The titration experiment was conducted as reported previously (16).

Immunoblotting

Control (GM23964, Coriell Institute for Medical Research) and $DHTKD1^{R715C/G729R}$ patient-derived fibroblasts (a gift of Dr. Jose E. Abdenur, University of California, Irvine) were cultured in Dulbecco's modified Eagle's cell culture medium supplemented with 10% fetal bovine serum. The samples for the immunoblot analysis of AMOXAD patient's fibroblasts in Fig. 1*A* were exactly as reported in (3). Cells were lysed in RIPA lysis and extraction buffer supplemented with protease inhibitor mixture and centrifuged 10 min at 12,000 × *g* at 4 °C, and total protein was determined by the BCA method. Proteins were separated on a Bolt™ 4–12% Bis-TrisPlus Gel, blotted onto a nitrocellulose membrane, and were detected by using the following primary antibodies against *DHTKD1*-encoded protein (GTX32561, Lot no. 821800318, GeneTex), citrate synthase (GT1761) (GTX628143, Lot no. 41113, GeneTex), and glyceraldehyde-3-phosphate dehydrogenase (H00002597-D01P, Lot no. EB071, RRID:AB_1503253, Abnova). Proteins were detected and visualized using IRDye 800CW or IRDye 680RD secondary antibodies (LI-COR Biosciences, Lincoln, NE) and Image Studio Lite software (version 5.2, LI-COR Biosciences). Equal loading was checked by Ponceau S Staining Solution and citrate synthase and glyceraldehyde-3-phosphate dehydrogenase signals.

Thermal shift assay

Thermal shift assay for E1a and G729R E1a purified by Houten and co-workers (54) was performed using QuantStudio 3 real-time PCR system (Applied Biosystems). Purified proteins were diluted to a final concentration of 0.5 mg/ml in 100 mM KH_2PO_4 (pH 7.2) containing 1 mM $MgCl_2$, 0.21 mM ThDP, and 20% glycerol. A 17.5-μl aliquot of protein was mixed with 2.5 μl of 8× SYPRO Orange in a final volume of 20 μl. The 8× SYPRO Orange was prepared by diluting the dye by 250-fold in H_2O. The reactions were kept at 25 °C for 2 min, and then the temperature was increased from 25 to 95 °C at a rate of 0.05 °C/s. The change in the fluorescence intensities of SYPRO Orange was monitored as a function of temperature and was analyzed by Protein Thermal Shift Software 1.3. Each reaction was performed in five replicates.

Mass spectrometry

(i) HDX–MS analysis was conducted as described by us earlier using a 7T Bruker Daltonics FT–MS instrument (16, 17, 40–42). Peptides were identified from nondeuterated samples by a customized program DXgest (43), which matches experimental peptide mass with theoretically-generated peptic peptide mass by using statistical data for the pepsin cleavage pattern under H/D exchange. Mass tolerance was set at 2.0 ppm. H/D exchange data for each individual peptide at various time points were processed using QUDeX-MS (44) and HX-Express (45). No back-exchange correction was needed for the purpose of comparative analysis. All time points were run in duplicates. The deuterium uptake level and deuterium incorporation were plotted with the mean value of two independent experiments.

(ii) For CL–MS analysis of the E1a·E2o and G729R E1a·E2o binary subcomplexes, the CDI was used. First, the E1a (1 nmol, 33 μM subunits) in 20 mM K_2HPO_4 (pH 7.5) containing 0.5 mM ThDP, 1 mM $MgCl_2$, 0.15 M NaCl, and 10% glycerol was mixed in 15 μl with E2o (1 nmol, 33 μM subunits) in the same buffer system. After 30 min of incubation at 20 °C, 1 μl of CDI (1 M) dissolved in DMSO was added, and the cross-linking reaction was conducted at 15 °C for 45 min. To quench the reaction, the reaction mixture was diluted to 50 μl with reaction buffer above, and 1 M Tris·HCl (pH 8.0) was added to a final concentration of 20 mM. Cross-linked E1a–E2o was identified by SDS-PAGE (7.5%).

Next, cross-linked samples were subjected to tryptic and Glu-C in-solution double digestion. An aliquot containing 1 nmol of the total protein was withdrawn from each reaction mixture and was placed into 70 μl of 8 M urea in 100 mM NH_4HCO_3, and the samples were incubated at 60 °C. After 20 min of incubation, 2 μl of 200 mM DTT was added, and the samples were incubated for an additional 40 min. Next, 3.5 μl of 200 mM iodoacetamide was added, and the samples were incubated at room temperature in the dark for 30 min. Then, 1 μl of 200 mM DTT was added, with a subsequent dilution of the reaction mixture with 0.85 ml of 100 mM NH_4HCO_3. The Glu-C digestion was carried out at 50:1 protein to Glu-C (w/w) ratio at 37 °C. After 4 h of incubation, the reaction mixtures were subjected to tryptic digestion at 100:1 protein to trypsin (w/w) ratio at 37 °C. After overnight digestion, the reaction was terminated by addition of 2 μl of 95% formic acid. Digested samples were desalted on a SepPak SPE C-18 column, dried using a SpeedVac centrifuge (Savant), and then dissolved in 100 μl of 20% acetonitrile (0.05% formic acid).

Peptide enrichment was carried out by using an SCX trap cartridge. The enriched peptides were desalted by a SepPak SPE C-18 column and were dried using a SpeedVac centrifuge. Cross-linked peptides were analyzed by nano-LC-MS/MS (Dionex Ultimate 3000 RLSC nanosystem interfaced with Q Exactive HF (Thermo Fisher Scientific)) as reported by us earlier (16) and were evaluated by using software tool Merox 1.6.6 (46). Samples were loaded onto a self-packed 100-μm by 2-cm trap (Magic C18AQ; 5 μm and 200 Å; Michrom Bioresources, Inc.) and washed with buffer A (0.1% TFA) for 5 min at a flow rate of 10 μl/min. The trap was brought in-line with the analytical column (self-packed Magic C18AQ; 3 μm and 200 Å; 75 μm by 50 cm), and peptides were eluted at 300 nl/min using a segmented linear gradient of 4–15% solution A in 30 min (solution A, 0.2% formic acid; solution B, 0.16% formic acid, 80% acetonitrile), 15–25% solution B in 40 min, 25–50% solution B in 44 min, and 50–90% solution B in 11 min. Mass spectrometric data were acquired using a data-dependent acquisition pro-

cedure with a cyclic series of a full scan with a resolution of 120,000, followed by MS/MS (higher-energy C-trap dissociation; relative collision energy, 27%) of the 20 most intense ions and a dynamic exclusion duration of 20 s. LC-MS/MS peak lists were generated using the ProteoWizard 3.0.18156 (48) software package and searched against the SwissProt database (proteome ID: UP000000558, search was done by using searchGUI-3.3.117 incorporated with Peptideshaker 1.16.42 (49, 50)). Search parameters were as follows: fragment mass error, 20 ppm; parent mass error, 5 ppm; fixed modification, carbamidomethylation on cysteine; potential modifications during initial search, methionine oxidation and acetylation on protein N termini and up to one missed tryptic cleavage. This search showed that no contaminant protein above 5% was present in the sample. Cross-links were evaluated using the software tool Merox 1.6.6 (46) with the following parameters: precursor 5 ppm; fragment 15 ppm mass accuracy; CDI was set as cross-linker. Only Lys–Lys cross-linked peptides were analyzed. The cross-linked peptides were manually validated, and the results with false discovery rate (FDR) <0.01 limit were analyzed (FDR was calculated by Merox software). The results were visualized online using the XVIS website (51). The MS proteomics data have been deposited to the ProteomeXchange Consortium (52) via the PRIDE (53) partner repository with the dataset identifier PXD017792. In Figs. S7–S10 are presented all MS/MS spectra for cross-links identified in E1a, G729R E1a, E1a·E2o subcomplex, and G729R E1a·E2o subcomplex.

Data availability

The MS proteomics data have been deposited to the ProteomeXchange Consortium via the PRIDE partner repository with the dataset identifier PXD017792. All remaining data are contained within the article and supporting information.

Author contributions—X. Z., N. S. N., J. L., S. H., M. B. L., G. J. G., O. O., and F. J. conceptualization; X. Z., J. L., S. H., and F. J. resources; X. Z., N. S. N., J. L., S. H., M. B. L., G. J. G., O. O., and A. A. data curation; X. Z., N. S. N., M. B. L., G. J. G., O. O., and A. A. software; X. Z., N. S. N., and J. L. formal analysis; X. Z., O. O., A. A., and F. J. supervision; X. Z., S. H., M. B. L., and F. J. funding acquisition; X. Z., N. S. N., J. L., S. H., M. B. L., G. J. G., O. O., A. A., and B. N. validation; X. Z., N. S. N., J. L., S. H., M. B. L., G. J. G., O. O., A. A., B. N., and R. B. investigation; X. Z., N. S. N., J. L., S. H., M. B. L., G. J. G., R. B., and F. J. visualization; X. Z., N. S. N., J. L., S. H., M. B. L., G. J. G., O. O., A. A., B. N., R. B., and F. J. methodology; X. Z., N. S. N., J. L., S. H., M. B. L., G. J. G., O. O., A. A., and F. J. writing-original draft; S. H. and M. B. L. project administration.

References

1. Danhauser, K., Sauer, S. W., Haack, T. B., Wieland, T., Staufner, C., Graf, E., Zschocke, J., Strom, T. M., Traub, T., Okun, J. G., Meitinger, T., Hoffmann, G. F., Prokisch, H., and Kölker, S. (2012) *DHTKD1* mutations cause 2-aminoadipic and 2-oxoadipic aciduria. *Am. J. Hum. Genet.* **91,** 1082–1087 CrossRef Medline
2. Stiles, A. R., Venturoni, L., Mucci, G., Elbalalesy, N., Woontner, M., Goodman, S., and Abdenur, J. E. (2016) New cases of *DHTKD1* mutations in patients with 2-ketoadipic aciduria. *JIMD Rep.* **25,** 15–19 CrossRef Medline
3. Hagen, J., te Brinke, H., Wanders, R. J., Knegt, A. C., Oussoren, E., Hoogeboom, A. J., Ruijter, G. J., Becker, D., Schwab, K. O., Franke, I., Duran, M., Waterham, H. R., Sass, J. O., and Houten, S. M. (2015) Genetic basis of α-aminoadipic and α-ketoadipic aciduria. *J. Inherit. Metab. Dis.* **38,** 873–879 CrossRef Medline
4. Xu, W. Y., Gu, M. M., Sun, L. H., Guo, W. T., Zhu, H. B., Ma, J. F., Yuan, W. T., Kuang, Y., Ji, B. J., Wu, X. L., Chen, Y., Zhang, H. X., Sun, F. T., Huang, W., Huang, L., *et al.* (2012) A nonsense mutation in *DHTKD1* causes Charcot-Marie-Tooth type 2 in a large Chinese pedigree. *Am. J. Hum. Genet.* **91,** 1088–1094 CrossRef Medline
5. Xu, W., Zhu, H., Gu, M., Luo, Q., Ding, J., Yao, Y., Chen, F., and Wang, Z. (2013) DHTKD1 is essential for mitochondrial biogenesis and function maintenance. *FEBS Lett.* **587,** 3587–3592 CrossRef Medline
6. Xu, W. Y., Zhu, H., Shen, Y., Wan, Y. H., Tu, X. D., Wu, W. T., Tang, L., Zhang, H. X., Lu, S. Y., Jin, X. L., Fei, J., and Wang, Z. G. (2018) DHTKD1 deficiency causes Charcot-Marie-Tooth disease in mice. *Mol. Cell. Biol.* **38,** e00085-18 CrossRef Medline
7. Sherrill, J. D., Wang, K. C., Wen, T., Chamberlin, A., Stucke, E. M., Collins, M. H., Abonia, J. P., Peng, Y., Wu, Q., Putnam, P. E., Dexheimer, P. J., Aronow, B., Kottyan, L. C., Kaufman, K. M., Harley, J. B., *et al.* (2018) Whole-exome sequencing uncovers oxidoreductases DHTKD1 and OGDHc as linkers between mitochondrial dysfunction and eosinophilic esophagitis. *JCI Insight* **3,** e99922 CrossRef Medline
8. Biagosch, C., Ediga, R. D., Hensler, S. V., Faerberboeck, M., Kuehn, R., Wurst, W., Meitinger, T., Kolker, S., and Sauer, S. (2017) Elevated glutaric acid levels in Dhtkd1-/Gcdh- double knockout mice challenge our current understanding of lysine metabolism. *Biochim. Biophys. Acta Mol. Basis Dis.* **1863,** 2220–2228 CrossRef Medline
9. Leandro, J., Dodatko, T., Aten, J., Nemeria, N. S., Zhang, X., Jordan, F., Hendrickson, R. C., Sanchez, R., Yu, C., DeVita, R. J., and Houten, S. M. (2020) DHTKD1 and OGDH display substrate overlap in cultured cells and form a hybrid 2-oxo acid dehydrogenase complex *in vivo*. *Human Mol. Gen.* **29,** 1168–1179 CrossRef Medline
10. Nemeria, N. S., Gerfen, G., Yang, L., Zhang, X., and Jordan, F. (2018) Evidence for functional and regulatory cross-talk between the tricarboxylic acid cycle 2-oxoglutarate dehydrogenase complex and 2-oxoadipate dehydrogenase on the L-lysine, L- hydroxylysine and L-tryptophan degradation pathways from studies *in vitro. Biochim. Biophys. Acta Bioenerg.***1859**, 932–939 CrossRef Medline
11. Nemeria, N. S., Gerfen, G., Nareddy, P. R., Yang, L., Zhang, X., Szostak, M., and Jordan, F. (2018) The mitochondrial 2-oxoadipate and 2-oxoglutarate dehydrogenase complexes share their E2 and E3 components for their function and both generate reactive oxygen species. *Free Radic. Biol. Med.* **115,** 136–145 CrossRef Medline
12. Jordan, F., Nemeria, N., and Gerfen, G. (2019) Human 2-oxoglutarate dehydrogenase and 2-oxoadipate dehydrogenase both generate superoxide/H_2O_2 in a side-reaction and each could contribute to oxidative stress in mitochondria. *Neurochem. Res.* **44,** 2325–2335 CrossRef Medline
13. Balakrishnan, A., Jordan, F., and Nathan, C. F. (2013) Influence of allosteric regulators on individual steps in the reaction catalyzed by *Mycobacterium tuberculosis* 2-hydroxy-3-oxoadipate synthase. *J. Biol. Chem.* **288,** 21688–21702 CrossRef Medline
14. Nemeria, N. S., Gerfen, G., Guevara, E., Reddy Nareddy, P. R., Szostak, M., and Jordan, F. (2017) The human Krebs cycle 2-oxoglutarate dehydrogenase complex creates an additional source of superoxide/hydrogen peroxide from 2-oxoadipate as alternative source. *Free Radic. Biol. Med.* **108,** 644–654 CrossRef Medline
15. Nemeria, N. S., Ambrus, A., Patel, H., Gerfen, G., Adam-Vizi, V., Tretter, L., Zhou, J., Wang, J., and Jordan, F. (2014) Human 2-oxoglutarate dehydrogenase complex E1 component forms a thiamin-derived radical by aerobic oxidation of the enamine intermediate. *J. Biol. Chem.* **289,** 29859–29873 CrossRef Medline
16. Zhou, J., Yang, L., Ozohanics, O., Zhang, X., Wang, J., Ambrus, A., Arjunan, P., Brukh, R., Nemeria, N. S., Furey, W., and Jordan, F. (2018) A multipronged approach unravels unprecedented protein–protein interactions in the human 2-oxoglutarate dehydrogenase multienzyme complex. *J. Biol. Chem.* **293,** 19213–19227 CrossRef Medline
17. Wang, J., Nemeria, N. S., Chandrasekhar, K., Kumaran, S., Arjunan, P., Reynolds, S., Calero, G., Brukh, R., Kakalis, L., Furey, W., and Jordan, F. (2014) Structure and function of the catalytic domain of the dihydrolipoy-

lacetyltransferase component in the *Escherichia coli* pyruvate dehydrogenase complex. *J. Biol. Chem.* **289,** 15215–15230 CrossRef Medline
18. Chakraborty, J., Nemeria, N. S., Farinas, E., and Jordan, F. (2018) Catalysis of transthiolacylation in the active centers of dihydrolipoamide acyltransferase components of 2-oxo acid dehydrogenase complexes. *FEBS Open Bio.* **8,** 880–896 CrossRef Medline
19. Balakrishnan, A., Nemeria, N. S., Chakraborty, S., Kakalis, L., and Jordan, F. (2012) Determination of pre-steady-state rate constants on the *Escherichia coli* pyruvate dehydrogenase complex reveals that loop movement controls the rate-limiting step. *J. Am. Chem. Soc.* **134,** 18644–18655 CrossRef Medline
20. Song, J., and Jordan, F. (2012) Inter-chain acetyl transfer in the E2 component of bacterial pyruvate dehydrogenase suggests a model with different roles for each chain in a trimer of the homooligomeric component. *Biochemistry* **51,** 2795–2803 CrossRef Medline
21. Parthasarathy, A., Pierik, A. J., Kahnt, J., Zelder, O., and Buckel, W. (2011) Substrate specificity of 2-hydroxyglutaryl-CoA dehydratase from *Clostridium symbiosum*: toward a bio-based production of adipic acid. *Biochemistry* **50,** 3540–3550 CrossRef Medline
22. Konermann, L., Pan, J., and Liu, Y.-H. (2011) Hydrogen exchange mass spectrometry for studying protein structure and dynamics. *Chem. Soc. Rev.* 40, 1224–1234 CrossRef Medline
23. Zhou, J., Yang, L., DeColli, A., Freel Meyers, C., Nemeria, N. S., and Jordan, F. (2017) Conformational dynamics of 1-deoxy-D-xylulose 5-phosphate synthase on ligand binding revealed by H/D exchange MS. *Proc. Natl. Acad. Sci. U.S.A.* **114,** 9355–9360 CrossRef Medline
24. DeColli, A. A., Zhang, X., Heflin, K. L., Jordan, F., and Freel Meyers, C. L. (2019) Active site histidines link conformational dynamics with catalysis on the anti-infective target 1-deoxy-D-xylulose 5-phosphate synthase. *Biochemistry* **58,** 4970–4982 CrossRef Medline
25. Wagner, T., Bellinzoni, M., Wehenkel, A., O'Hare, H. M., and Alzari, P. M. (2011) Functional plasticity and allosteric regulation of α-ketoglutarate decarboxylase in central mycobacterial metabolism. *Chem. Biol.* **18,** 1011–1020 CrossRef Medline
26. Wagner, T., Barilone, N., Alzari, P. M., and Bellinzoni, M. (2014) A dual conformation of the post-decarboxylation intermediate is associated with distinct enzyme states in mycobacterial KGD (α-ketoglutarate decarboxylase). *Biochem. J.* **457,** 425–434 CrossRef Medline
27. Bezerra, G. A., Foster, W. R., Bailey, H. J., Hicks, K. G., Sauer, S. W., Dimitrov, B., Okun, J. G., Rutter, J., Kölker, S., and Yue, W. W. (2020) Crystal structure and interaction studies of human DHTKD1 provide insight into a mitochondrial megacomplex in lysine metabolism. *bioRxiv* CrossRef
28. Derosier, D. J., Oliver, R. M., and Reed, L. J. (1971) Crystallization and preliminary structural analysis of dihydrolipoyltranssuccinylase, the core of the 2-oxoglutarate dehydrogenase complex. *Proc. Natl. Acad. Sci. U.S.A.* **68,** 1135–1137 CrossRef Medline
29. Knapp, J. E., Mitchell, D. T., Yazdi, M. A., Ernst, S. R., Reed, L. J., and Hackert, M. L. (1998) Crystal structure of the truncated cubic core component of the *Escherichia coli* 2 oxoglutarate dehydrogenase multienzyme complex. *J. Mol. Biol.* **280,** 655–668 CrossRef Medline
30. Knapp, J. E., Carroll, D., Lawson, J. E., Ernst, S. R., Reed, L. J., and Hackert, M. L. (2000) Expression, purification, and structural analysis of the trimeric form of the catalytic domain of the *Escherichia coli* dihydrolipoamide succinyltransferase. *Protein Sci.* **9,** 37–48 CrossRef Medline
31. Suzuki, K., Adachi, W., Yamada, N., Tsunoda, M., Koike, K., Koike, M., Sekiguchi, T., and Tekénaka, A. (2002) Crystallization and preliminary X-ray analysis of the full-size cubic core of pig 2-oxoglutarate dehydrogenase complex. *Acta Crystallogr. D Biol. Crystallogr.* **58,** 833–835 CrossRef Medline
32. Wagenknecht, T., Grassucci, R., and Schaak, D. (1990) Cryoelectron microscopy of frozen-hydrated α-ketoacid dehydrogenase complexes from *Escherichia coli*. *J. Biol. Chem.* **265,** 22402–22408 Medline
33. Wagenknecht, T., Grassucci, R., Berkowitz, J., and Forneris, C. (1992) Configuration of interdomain linkers in pyruvate dehydrogenase complex of *Escherichia coli* as determined by cryoelectron microscopy. *J. Struct. Biol.* **109,** 70–77 CrossRef Medline
34. Murphy, G. E., and Jensen, G. J. (2005) Electron cryotomography of the *E. coli* pyruvate and 2-oxoglutarate dehydrogenase complexes. *Structure* **13,** 1765–1773 CrossRef Medline
35. Byron, O., and Lindsay, J. G. (2017) The pyruvate dehydrogenase complex and related assemblies in health and disease. *Subcell. Biochem.* **83,** 523–550 CrossRef Medline
36. Hage, C., Iacobucci, C., Rehkamp, A., Arlt, C., and Sinz, A. (2017) The first zero-length mass spectrometry-cleavable cross-linker for protein structure analysis. *Angew. Chem. Int. Ed. Engl.* **56,** 14551–14555 CrossRef Medline
37. Rappsilber, J. (2011) The beginning of a beautiful friendship: cross-linking/mass spectrometry and modelling of proteins and multi-protein complexes. *J. Struct. Biol.* **173,** 530–540 CrossRef Medline
38. Chakraborty, J., Nemeria, N. S., Zhang Xu Nareddy, P. R., Szostak, M., Farinas, E., and Jordan, F. (2019) Engineering 2-oxoglutarate dehydrogenase to a 2-oxo aliphatic dehydrogenase complex by optimizing consecutive components. *AIChE J.* **66,** CrossRef
39. Frank, R. A., Price, A. J., Northrop, F. D., Perham, R. N., and Luisi, B. F. (2007) Crystal structure of the E1 component of the *Escherichia coli* 2-oxoglutarate dehydrogenase multienzyme complex. *J. Mol. Biol.* **368,** 639–651 CrossRef Medline
40. Wang, J., Kumaran, S., Zhou, J., Nemeria, N. S., Tao, H., Kakalis, L., Park, Y.-H., Birkaya, B., Patel, M. S., and Jordan, F. (2015) Elucidation of the interaction loci of the human pyruvate dehydrogenase complex E2·E3BP core with pyruvate dehydrogenase kinase 1 and kinase 2 by H/D exchange mass spectrometry and nuclear magnetic resonance. *Biochemistry* **54,** 69–82 CrossRef Medline
41. Arjunan, P., Wang, J., Nemeria, N. S., Reynolds, S., Brown, I., Chandrasekhar, K., Calero, G., Jordan, F., and Furey, W. (2014) Novel binding motif and new flexibility revealed by structural analyses of a pyruvate dehydrogenase-dihydrolipoyl acetyltransferase subcomplex from the *Escherichia coli* pyruvate dehydrogenase multienzyme complex. *J. Biol. Chem.* **289,** 30161–30176 CrossRef Medline
42. Ambrus, A., Wang, J., Mizsei, R., Zambo, Z., Torocsik, B., Jordan, F., and Adam-Vizi, V. (2016) Structural alterations induced by ten disease-causing mutations of human dihydrolipoamide dehydrogenase analyzed by hydrogen/deuterium-exchange mass spectrometry: implications for structural basis of E3 deficiency. *Biochim. Biophys. Acta* **1862,** 2098–2109 CrossRef Medline
43. Hamuro, Y., Coales, S. J., Molnar, K. S., Tuske, S. J., and Morrow, J. A. (2008) Specificity of immobilized porcine pepsin in H/D exchange compatible conditions. *Rapid Commun. Mass Spectrom.* **22,** 1041–1046 CrossRef Medline
44. Salisbury, J. P., Liu, Q., and Agar, J. N. (2014) QUDeX-MS: hydrogen/deuterium exchange calculation for mass spectra with resolved isotopic fine structure. *BMC Bioinformatics* **15,** 403 CrossRef Medline
45. Weis, D. D., Engen, J. R., and Kass, I. J. (2006) Semi-automated data processing of hydrogen exchange mass spectra using HX-Express. *J. Am. Soc. Mass Spectrom.* **17,** 1700–1703 CrossRef Medline
46. Götze, M., Pettelkau, J., Fritzsche, R., Ihling, C. H., Schäfer, M., and Sinz, A. (2015) Automated assignment of MS/MS cleavable cross-links in protein 3D-structure analysis. *J. Am. Soc. Mass. Spectrom.* **26,** 83–97 CrossRef Medline
47. Roy, A., Kucukural, A., and Zhang, Y. (2010) I-TASSER: a unified platform for automated protein structure and function prediction. *Nat. Protoc.* **5,** 725–738 CrossRef Medline
48. Chambers, M. C., Maclean, B., Burke, R., Amodei, D., Ruderman, D. L., Neumann, S., Gatto, L., Fischer, B., Pratt, B., Egertson, J., Hoff, K., Kessner, D., Tasman, N., Shulman, N., Frewen, B., *et al.* (2012) A cross-platform toolkit for mass spectrometry and proteomics. *Nat. Biotechnol.* **30,** 918–920 CrossRef Medline
49. Barsnes, H., and Vaudel, M. (2018) SearchGUI: a highly adaptable common interface for proteomics search and de novo engines. *J. Proteome Res.* **17,** 2552–2555 CrossRef Medline
50. Vaudel, M., Burkhart, J. M., Zahedi, R. P., Oveland, E., Berven, F. S., Sickmann, A., Martens, L., and Barsnes, H. (2015) PeptideShaker enables reanalysis of MS-derived proteomics data sets. *Nat. Biotechnol.* **33,** 22–24 CrossRef Medline
51. Grimm, M., Zimniak, T., Kahraman, A., and Herzog, F. (2015) *xVis*: a web server for the schematic visualization and interpretation of crosslink-derived spatial restraints. *Nucleic Acids Res.* **43,** W362–W369 CrossRef Medline

52. Deutsch, E. W., Csordas, A., Sun, Z., Jarnuczak, A., Perez-Riverol, Y., Ternent, T., Campbell, D. S., Bernal-Llinares, M., Okuda, S., Kawano, S., Moritz, R. L., Carver, J. J., Wang, M., Ishihama, Y., Bandeira, N., *et al.* (2017) The ProteomeXchange Consortium in 2017: supporting the cultural change in proteomics public data deposition. *Nucleic Acids Res.* **45,** D1100–D1106 CrossRef Medline
53. Perez-Riverol, Y., Csordas, A., Bai, J., Bernal-Llinares, M., Hewapathirana, S., Kundu, D. J., Inuganti, A., Griss, J., Mayer, G., Eisenacher, M., Pérez, E., Uszkoreit, J., Pfeuffer, J., Sachsenberg, T., Yilmaz, S., *et al.* (2019) The PRIDE database and related tools and resources in 2019: improving support for quantification data. *Nucleic Acids Res.* **47,** D442–D450 CrossRef Medline
54. Leandro, J., Khamrui, S., Wang, H., Suebsuwong, C., Nemeria, N. S., Huynh, K., Moustakim, M., Secor, C., Wang, M., Dodatko, T., Stauffer, B., Wilson, C. G., Yu, C., Arkin, M. R., Jordan, F., *et al.* (2020) Inhibition and crystal structure of the human DHTKD1-thiamin diphosphate complex. *bioRxiv.* CrossRef